Investigating Isotropy in Atmospheric Turbulence Using Large Eddy Simulations

by

Mohammad Mohammadifar

A thesis
presented to the University of Waterloo
in fulfillment of the
thesis requirement for the degree of
Master of Mathematics
in
Applied Mathematics

Waterloo, Ontario, Canada, 2026

© Mohammad Mohammadifar 2026

Author's Declaration

I hereby declare that I am the sole author of this thesis. This is a true copy of the thesis, including any required final revisions, as accepted by my examiners.

I understand that my thesis may be made electronically available to the public.

Abstract

Turbulence plays a key role in many atmospheric and engineering flows, but understanding how it becomes isotropic under different conditions is still a challenge. In this thesis, we use the WRF model in idealized mode to explore how turbulence evolves in four setups: two driven by buoyancy (convective boundary layer and plume) and two by shear (random and bubble-perturbed Shear). We analyze anisotropy of the eddy dissipation using eddy-viscosity-based metrics, comparing how different forcing mechanisms and spatial resolutions affect the development and isotropization of turbulence. Buoyancy-driven cases showed smoother, more gradual transitions to isotropy, while shear-driven cases featured stronger bursts, persistent anisotropy, and slower convergence in time, especially at low resolution. It can also be understood that vertical velocity is more anisotropic in buoyancy-driven cases, while vertical shear dominates in shear-driven cases. These results highlight how both physical forcing and resolution shape the anisotropy of turbulence and point to important considerations for model setup in future turbulence studies.

Acknowledgements

I want to start by thanking my supervisor, Michael Waite. This thesis wouldn't have happened without his support. I appreciate everything he did during my master's program, especially his patience and guidance. His help was invaluable. I hope Mike and his family are doing well. I would like to thank my committee, Francis Poulin and Jean-Pierre Hickey, for their time and help. A big thank you to my wonderful friends and family for your endless love and support! You all mean so much to me! This research was made possible thanks to the generous support of the Digital Research Alliance of Canada.

Dedication

This is dedicated to the one I love.

Table of Contents

Author's Declaration ii

Abstract iii

Acknowledgements iv

Dedication v

List of Figures viii

List of Tables x

1 Introduction 1

1.1 Background and Motivation 1

1.2 Turbulence and Isotropy in Atmospheric Flows 3

1.2.1 Kolmogorov Theory and Inertial Range Assumptions 3

1.2.2 Directional Dependence of Dissipation 4

1.2.3 When and Where Isotropy Breaks Down in Stratified or Sheared Flows 5

1.3 Large Eddy Simulation 6

1.3.1 Overview 6

1.3.2 Eddy Viscosity Models: Smagorinsky and TKE-Based Approaches . 8

1.4 Idealized Turbulent Flow Configurations 9

1.5 Dissipation Matrix and Isotropy Diagnostics . . . 10
1.6 Objectives . . . 12

2 Methodology **13**
2.1 Overview . . . 13
2.2 WRF Model and Computational Framework . . . 13
2.2.1 Vertical Coordinate System . . . 14
2.2.2 Governing Equations . . . 14
2.2.3 Richardson Number and Stability Criteria . . . 17
2.3 Domain Setup, Resolution, and Initialization . . . 17
2.4 Physical Settings . . . 23
2.5 Isotropy Diagnostics . . . 23
2.5.1 Dissipation Ratios in Isotropic Turbulence (Taylor's Ratios) . . . 23
2.5.2 Extension to LES with Eddy Viscosity . . . 24

3 Results **26**
3.1 Convective Boundary Layer . . . 26
3.2 Plume . . . 31
3.3 Randomly Perturbed Stratified Shear flow . . . 38
3.4 Locally Perturbed Stratified Shear FLow . . . 44

4 Conclusion **51**

References **54**

List of Figures

2.1 Initial potential temperature profiles for each simulation. The CBL profile is 2 km. The plume case includes a warm anomaly at 5 km. Both bubble shear and random shear share the same tanh-shaped profile. 21

2.2 Initial horizontal (x-direction) velocity profiles. The CBL and plume cases start from rest, while the shear cases have a tanh profile centred near 5 km to induce shear. 22

3.1 Magnitude of total vorticity contour of CBL simulation during the fully developed stage for four selected times. 27

3.2 Potential Temperature contour of CBL simulation during fully developed stage for four selected times. 28

3.3 Temporal evolution of total dissipation rate in the CBL simulation. 29

3.4 Anisotropy matrix components(ϵ_{ij}) in the CBL simulation, comparing high- and low-resolution cases. Top: diagonal elements with theoretical value 2/15. Bottom: off-diagonal elements with theoretical value 1/10. 30

3.5 Evolution of total anisotropy χ_ϵ in log scale for high- and low-resolution CBL simulations. 31

3.6 Magnitude of total vorticity contour of plume simulation during the fully developed stage for four selected times. 33

3.7 Potential Temperature contour of plume simulation during fully developed stage for four selected times. 34

3.8 Temporal evolution of total dissipation rate in the plume simulation. 35

3.9 Anisotropy matrix components, ϵ_{ij}, in the plume simulation, comparing high- and low-resolution results. Top: diagonal elements with reference line at 2/15. Bottom: off-diagonal elements with reference to 1/10. 36

3.10 Evolution of total anisotropy χ_ϵ in log scale for high- and low-resolution plume simulations. 37

3.11 Magnitude of total vorticity contour of randomly perturbed simulation for four selected times. 39

3.12 Potential Temperature contour of randomly perturbed simulation for four selected times. 40

3.13 Time evolution of total dissipation rate ϵ_{tot} in the randomly perturbed simulation. 41

3.14 Anisotropy matrix components in the randomly perturbed simulation. Top: diagonal elements (reference line at 2/15). Bottom: off-diagonal elements (reference line at 1/10). 42

3.15 Temporal evolution of total anisotropy χ_ϵ (log scale) for high- and low-resolution randomly perturbed simulations. 43

3.16 Magnitude of total vorticity contour of the shear-driven simulation for four selected times. 45

3.17 Potential temperature contour of the shear-driven simulation for four selected times. 46

3.18 Time evolution of total dissipation rate ϵ_{tot} in the shear-driven simulation. 47

3.19 Anisotropy matrix components in the shear-driven simulation. Top: diagonal elements (reference line at 2/15). Bottom: off-diagonal elements (reference line at 1/10). 48

3.20 Temporal evolution of total anisotropy χ_ϵ (log scale) for high- and low-resolution shear-driven simulations. 49

List of Tables

2.1 Simulation configurations for each idealized case at low and high resolution. 18
2.2 Simulation setup and initial conditions for each case. 20

Chapter 1

Introduction

1.1 Background and Motivation

Atmospheric turbulence plays a central role in controlling the transport of momentum, heat, and tracers in the lower atmosphere [Wyngaard, 2010]. From microscale eddies that mix pollutants near the surface to larger turbulent plumes rising in convective conditions, turbulence underpins many of the key processes in weather and climate dynamics. In boundary-layer meteorology [Stull, 2006], the complexity and multiscale nature of turbulence pose major challenges to both theoretical understanding and numerical modelling. Despite significant advances, many questions remain about how accurately we can characterize turbulent flows, especially in regimes where the underlying assumptions of turbulence theory are stretched [Briggs, 1985].

A cornerstone of classical turbulence theory is the notion that, at sufficiently small scales, turbulent statistics become independent of directions, a condition known as local isotropy. This concept underpins much of our understanding of how energy cascades from large, chaotic motions to smaller, dissipative ones [Kolmogorov, 1941]. Building upon the early theories of energy cascades, further developments offered a formal framework for describing isotropic turbulence through energy spectra and statistical descriptors, laying the groundwork for much of modern turbulence analysis [Marston and Tobias, 2022]. The assumption of isotropy in large eddy simulation (LES) models is important but needs to be examined closely. This assumption affects how we build models. For example, the eddy viscosity assumption states that horizontal and vertical viscosity are equal, creating a consistent relationship between stress and strain rate, much like the Navier-Stokes equations [Frisch, 1995]. Additionally, this assumption influences the choice and effectiveness of

subgrid-scale (SGS) models, such as the Smagorinsky model. These models may not accurately represent complex flows that vary in different directions, especially in areas affected by shear, such as boundary layers. Therefore, while the idea of isotropy helps in developing turbulence models, we must recognize its limits to accurately capture certain turbulent behaviours in real-world situations [Muralidharan and Menon, 2019]. SGS models, such as those based on eddy viscosity, often rely on the assumption that these small-scale motions are isotropic, allowing simplified parameterizations of unresolved dynamics.

However, isotropy is not a universal feature of all turbulent flows. Especially in stratified, sheared, or surface-layer environments, directional biases introduced by buoyancy, shear, or terrain can lead to persistent anisotropy even at relatively small scales. Some theoretical work has examined how and when isotropy breaks down, showing that departures from isotropy can persist well into the inertial range under certain physical forcings [Carter and Coletti, 2017]. Observational studies and numerical simulations have further confirmed that in the real atmosphere, especially under strongly stratified or organized shear conditions, turbulence may exhibit structure and anisotropy that violates classical assumptions [Stiperski and Calaf, 2017, Lang and Waite, 2019]. Recent studies have taken another look at this issue, paying closer attention to it than before. High-resolution simulations and analyses have demonstrated that large-scale, non-turbulent motions and spatial variability in surface properties can introduce spectral distortions, thereby challenging the validity of isotropy assumptions in turbulent flows [Sirigu et al., 2025]. Moreover, experiments in idealized and realistic terrains have revealed that model-based representations of turbulence often struggle to capture these effects, resulting in discrepancies between predicted and observed flow behaviour. These insights make us question how we use isotropy in numerical models and highlight the need for diagnostic tools that can quantify anisotropy more precisely [Mosso et al., 2025]. There is a strong reason to study isotropic analysis in idealized turbulence environments, where we can isolate different forcing mechanisms. We want to go beyond just assuming isotropy and actually measure it. To do this, we will use high-resolution simulations that capture a wide range of turbulent scales [Warhaft, 2000].

This thesis aims to systematically analyze isotropy in four idealized turbulent flows using large eddy simulation with the Weather Research and Forecasting model. By applying diagnostic tools that assess directional dissipation behaviour, the work seeks to clarify under what conditions isotropy can be expected, how it evolves across scales, and how sensitive it is to resolution, initial conditions, and forcings.

1.2 Turbulence and Isotropy in Atmospheric Flows

1.2.1 Kolmogorov Theory and Inertial Range Assumptions

Turbulence is characterized by a chaotic and multiscale structure in both space and time. Despite this inherent complexity, certain statistical symmetries can be identified and used to simplify its analysis. Among these, isotropy holds a central role. In the context of turbulence, a flow is considered isotropic when its statistical properties are invariant under arbitrary rotations and reflections of the coordinate system [Pope, 2000]. This means that, on average, no spatial direction is preferred over another, and the velocity fluctuations and their gradients are distributed uniformly across all directions. Richardson's cascade idea describes how energy in a turbulent flow moves from large scales to smaller ones. This concept relies on the assumption of local isotropy, which allows the energy transfer at each scale to be characterized by a single velocity and length scale. Big eddies transfer energy to smaller and smaller eddies by vortex stretching [Richardson, 1922]. This process continues until the eddies are so small that viscosity takes over and turns the kinetic energy into heat. The smallest scale where this happens is called the Kolmogorov scale. At this scale, the energy cascade does not behave like it does at larger scales. Instead, energy is dissipated because of viscosity [Wyngaard, 2010].

In contrast, anisotropic turbulence exhibits directional dependence in its statistics. This may arise due to Initial conditions and external anisotropic processes such as gravity, mean shear, or surface heterogeneity, which imprint preferred orientations onto the flow. Anisotropy can present itself in various forms, including elongated structures aligned with the mean flow and variations in energy distribution across different velocity components [Taylor, 1935]. It is important to distinguish between global isotropy and local isotropy [Germano et al., 1991]. Global isotropy refers to flows that are statistically uniform in all directions throughout the entire domain, which is a condition rarely met in geophysical flows. Local isotropy, however, is a more relaxed condition, wherein the small-scale motions become isotropic even if the larger-scale flow is anisotropic. This concept plays a key role in turbulence theory, particularly in the context of energy cascade dynamics [Chowdhuri and Banerjee, 2024]. In practical terms, isotropy assumptions simplify turbulence modelling by allowing scalar or simplified tensor representations of quantities like Reynolds stresses and dissipation rates. Many subgrid-scale models and diagnostic frameworks, including those employed in large eddy simulations, implicitly or explicitly rely on isotropy to close unresolved terms. Therefore, understanding the extent to which real atmospheric turbulence conforms to or deviates from isotropic behaviour is crucial for interpreting model results and developing physically consistent diagnostics [Stiperski et al., 2018].

1.2.2 Directional Dependence of Dissipation

The rate of kinetic energy dissipation per unit mass is typically described by the scalar:

$$\epsilon = 2\nu \left\langle s_{ij} s_{ij} \right\rangle ,$$

where ν is the kinematic viscosity, and s_{ij} is the strain rate matrix:

$$s_{ij} = \frac{1}{2} \left(\frac{\partial u_i}{\partial x_j} + \frac{\partial u_j}{\partial x_i} \right) .$$

Einstein's summation convention is used, where summation is implied for repeated indices, so this is a double sum with 9 terms. But since s_{ij} is symmetric, there are only 6 independent terms. This formulation captures the contribution of all velocity gradients to the total dissipation, but it does not indicate how dissipation is distributed across the gradients in different directions. To explore this, one can examine the individual terms inside the sum, such as s_{11}^2, s_{22}^2, s_{33}^2, and the cross terms such as s_{12}^2, s_{13}^2, and s_{23}^2 , which reflect how energy is dissipated due to gradients in specific directions. In isotropic turbulence, the statistical contributions of these terms are expected to follow specific ratios. For example, in isotropic conditions, the mean-square values of the diagonal and off-diagonal components of the strain rate tensor have known theoretical proportions. These reference values serve as benchmarks for identifying anisotropy [Hebert and de Bruyn Kops, 2006, Lang and Waite, 2019]. If the observed values deviate from these benchmarks, it suggests that the flow retains some directional bias in its small-scale structure, even in the dissipation range [Wang et al., 2021].

This distinction is important in LES, where the smallest resolved scales are modelled rather than directly computed. Many SGS models assume that turbulence is isotropic at the subgrid level. However, in atmospheric flows influenced by shear, stratification, or surface inhomogeneity, this assumption can break down [Reiter and Burns, 1966]. In such cases, the modelled dissipation may not accurately capture the directional structure of the true dissipation, leading to potential errors in the energy budget and flow dynamics. Therefore, analyzing the directional contributions to dissipation provides a useful diagnostic for assessing anisotropy in both real and simulated flows. It also offers insight into the limits of turbulence models that rely on isotropy assumptions at unresolved scales [Wyngaard, 2010].

1.2.3 When and Where Isotropy Breaks Down in Stratified or Sheared Flows

While isotropy serves as a convenient assumption in turbulence theory and modelling, it is well recognized that many real-world flows deviate significantly from this ideal. In the atmosphere, turbulence frequently develops under conditions that introduce strong directional biases, most notably due to stratification, convection, and mean shear. These influences not only affect the large-scale dynamics but can also imprint anisotropic characteristics on smaller scales, including those involved in energy dissipation [Chamecki and Dias, 2006].

Stratification, whether stable or unstable, imposes a vertical structure on the flow. In stably stratified environments, vertical motions are suppressed by buoyant forces, leading to turbulence that is flattened and elongated in the horizontal plane. This anisotropy may persist across a broad range of scales and can affect both the intensity and distribution of dissipation [Pumir et al., 2016]. In contrast, in unstable conditions such as those driven by surface heating, vertical motions are enhanced, but coherent structures like thermal plumes may still introduce directional features that depart from isotropic expectations [Stiperski et al., 2021]. These features manifest in various turbulent statistics. For example, anisotropic flows often show unequal variances in different velocity components, elevated skewness in scalar or velocity fields, and spectral energy distributions that vary with direction [Yokoyama and Takaoka, 2019]. In the dissipation range, anisotropy may appear as non-uniform directional contributions to the strain rate terms used in estimating dissipation. These statistical signatures indicate that even the smallest scales of motion can retain a memory of anisotropic forcing conditions from larger scales [Xiao and Senocak, 2022]. The persistence of anisotropy at small scales is often governed by dynamic length scales associated with stratification and shear. In stably stratified flows, the Ozmidov scale,

$$L_O = \left(\frac{\epsilon}{N^3}\right)^{1/2},$$

marks the smallest scale at which buoyancy effects are significant. Here, ϵ is the turbulent dissipation rate, and N is the Brunt–Väisälä frequency,

$$N = \left(\frac{g}{\theta}\frac{d\theta}{dz}\right)^{1/2},$$

where g is the acceleration due to gravity, θ is the potential temperature, and $\frac{d\theta}{dz}$ is the vertical potential temperature gradient. Below this scale, the flow becomes less affected by buoyancy, and isotropy is more likely to develop.

Shear is another dominant mechanism that breaks isotropy. When a mean velocity gradient exists, such as in a jet, shear layer, or boundary layer, turbulent structures become stretched and aligned along the direction of the flow. The resulting turbulence is highly anisotropic, with enhanced production of energy along specific axes and nonuniform dissipation rates. This is particularly evident in the atmospheric boundary layer, where wind shear interacts with surface roughness and thermal stratification to generate complex, anisotropic turbulent fields [Watanabe and Nagata, 2023]. In shear-dominated flows, the shear length scale is:

$$L_s = \left(\frac{\epsilon}{|s|^3} \right)^{1/2},$$

where $|s|$ is the magnitude of the mean, $|s| = \sqrt{2 s_{ij} s_{ij}}$. If the turbulence does not extend to scales smaller than L_O or L_s, anisotropy may persist down to the dissipation range, violating assumptions of local isotropy [Smyth and Moum, 2000]. Even in idealized numerical simulations, such as those performed under large eddy simulation frameworks, this anisotropy can persist. As such, diagnosing the extent and nature of isotropy in different flow regimes is critical. This diagnostics allows researchers to understand the limitations of classical turbulence theory in applied contexts and to identify which physical mechanisms are responsible for maintaining anisotropy across scales. This understanding is essential for refining modelling approaches and improving the predictive skill of atmospheric simulations, particularly in cases where standard assumptions may lead to systematic biases [Glegg and Devenport, 2017].

1.3 Large Eddy Simulation

1.3.1 Overview

LES is a turbulence modelling framework that resolves the largest, most energetic eddies in a turbulent flow while modelling the influence of the smaller, subgrid-scale motions. Unlike Reynolds-Averaged Navier–Stokes (RANS) approaches, which average turbulent fluctuations over all scales, LES directly captures the dynamic evolution of larger eddies that dominate energy transport. This makes LES particularly valuable in studies that require time-resolved representations of turbulence, such as this thesis. The central idea behind LES is scale separation. A low-pass spatial filter is applied to the governing equations of fluid motion to distinguish between resolved and unresolved scales. In the LES framework, a spatial filter is applied to the Navier–Stokes equations to separate the flow into large-scale (resolved) and small-scale (unresolved) components. Filtered quantities, which are

denoted by a tilde, are defined as:

$$\tilde{u}_i(\mathbf{x}) = \int G(\mathbf{x} - \mathbf{r}) u_i(\mathbf{r})\, d\mathbf{r},$$

where G is the filter function, and the integration is over the domain. This filtering operation enables explicit treatment of the large, energy-carrying eddies while modelling the influence of the smaller scales The filtered momentum equation takes the general form:

$$\frac{\partial \tilde{u}_i}{\partial t} + \tilde{u}_j \frac{\partial \tilde{u}_i}{\partial x_j} = -\frac{1}{\rho}\frac{\partial \tilde{p}}{\partial x_i} + \nu \frac{\partial^2 \tilde{u}_i}{\partial x_j^2} - \frac{\partial \tau_{ij}}{\partial x_j}, \tag{1.1}$$

where $\tilde{u}_i$ and $\tilde{p}$ denote the filtered velocity and pressure fields, ν is the kinematic viscosity, and τ_{ij} represents the SGS stress tensor, defined as:

$$\tau_{ij} = \widetilde{u_i u_j} - \tilde{u}_i \tilde{u}_j. \tag{1.2}$$

This SGS stress tensor encapsulates the impact of the unresolved scales on the resolved flow and must be modeled to close the system of equations. The choice of subgrid model is critical, as it affects the accuracy and physical realism of the LES results. LES occupies a middle ground between Direct Numerical Simulation (DNS), which resolves all scales but is computationally prohibitive for high Reynolds number flows, and RANS models, which don't resolve any turbulent fluctuations. By resolving a significant portion of the turbulent spectrum, LES allows for greater realism in representing energy-containing eddies and their interactions, particularly in unsteady or inhomogeneous flows. For this reason, LES has become a preferred approach for modelling atmospheric turbulence, especially for studies of boundary-layer dynamics and stratified turbulence where scale-dependent processes play a dominant role. In this thesis, LES is used not only to simulate turbulence, but also to investigate how turbulence behaves, such as how energy is dissipated and how isotropy varies—under different flow conditions and resolutions [Lopes et al., 2024].

The resolved scales represent the most energetic, dynamically significant structures of the flow. These scales may be anisotropic and highly sensitive to boundary and forcing conditions. They are directly computed by the numerical solver and include features such as convective plumes, shear layers, and turbulence bursts. The subgrid scales, by contrast, include the smaller motions that are not resolved but still affect energy dissipation. Though they contain less kinetic energy, they contribute critically to the energy cascade and dissipation [Meneveau and Katz, 2000].

The assumption of isotropy in many SGS models, although convenient, can fail in regimes with strong shear, stratification, or anisotropic forcing. In such flows, unresolved

motions may exhibit directional dependence, and standard models may underestimate or overestimate dissipation in certain directions. This can distort energy transfer between scales and reduce simulation accuracy [Supekar and Peacock, 2019]. For this reason, understanding the interaction between resolved and subgrid scales is essential, especially when analyzing flow anisotropy or developing improved turbulence diagnostics [Togni et al., 2019].

1.3.2 Eddy Viscosity Models: Smagorinsky and TKE-Based Approaches

To model the influence of unresolved SGS motions on resolved flow, LES relies on subgrid closure schemes. Among these, eddy viscosity models are a common approach. These models assume that the deviatoric part of the subgrid-scale stress tensor is proportional to the resolved strain rate tensor, in a manner analogous to the viscous stress in the Navier–Stokes equations.

$$\tau_{ij}^{\mathrm{SGS}} - \frac{1}{3}\tau_{kk}^{\mathrm{SGS}}\delta_{ij} = -2\nu_t \tilde{s}_{ij}, \tag{1.3}$$

where $\tilde{s}_{ij}$ is the resolved strain rate tensor and ν_t is the eddy viscosity. This representation captures the diffusive transport behaviour of small-scale turbulence and provides an eddy viscosity to model its dissipative effects on the larger, resolved flow [Pope, 2000]. One of the earliest and most influential SGS models is the Smagorinsky model [Smagorinsky, 1963], which defines the eddy viscosity as a function of local strain rate and grid spacing. The eddy viscosity in this approach is given by:

$$\nu_t = (C_s\Delta)^2|\tilde{s}|, \tag{1.4}$$

with C_s being the Smagorinsky constant, Δ the filter width (typically related to grid spacing), and $|\tilde{s}| = \sqrt{2\tilde{s}_{ij}\tilde{s}_{ij}}$ representing the magnitude of the resolved strain rate tensor. Despite its simplicity, the Smagorinsky model has proven effective in many applications and remains a baseline method in LES studies. However, its reliance on a fixed constant and its inability to account for backscatter (energy transfer from small to large scales) limit its accuracy, particularly in complex or transitional flows [Fröhlich et al., 2006].

An alternative class of models incorporates additional prognostic equations, most notably for subgrid-scale turbulent kinetic energy (TKE). In TKE-based models, the eddy viscosity is not prescribed directly, but is instead computed from the modelled subgrid energy:

$$\nu_t = C_k \Delta \sqrt{k_{\text{sgs}}}, \tag{1.5}$$

where k_{sgs} is the subgrid TKE and C_k is a model constant. In most implementations, including the one used in this study, k_{sgs} is obtained from a prognostic transport equation, which evolves the subgrid-scale energy based on production, dissipation, and diffusion terms. This method allows the model to dynamically adjust the subgrid energy in response to evolving flow conditions [Deardorff, 1980]. This approach allows the SGS turbulence to respond dynamically to local flow conditions, potentially improving performance in inhomogeneous or unsteady regions. It also enables better representation of the energetics of the unresolved scales, which is particularly important in stratified or shear-dominated flows. However, similar to other eddy-viscosity models, it does not capture energy backscatter from small to large scales, which can be important in transitional or weakly turbulent regions [Katopodes, 2019]. In this study, the LES simulations in WRF use a TKE-based SGS model, allowing for spatial and temporal variability in eddy viscosity.

LES provides a valuable research platform for probing the limits of isotropy in such regimes. Since it resolves large-scale motions directly, the model output can be used to diagnose directional variations in energy, strain, and dissipation [Sutherland et al., 2019]. This is particularly relevant for the present study, which focuses on quantifying the degree of isotropy in idealized but dynamically rich boundary-layer and stratified flow configurations. By applying LES in carefully controlled numerical experiments, the study is able to isolate key mechanisms that promote or inhibit isotropy, providing insights that are not easily accessible from observations or coarser models.

1.4 Idealized Turbulent Flow Configurations

Idealized simulations offer a simplified yet physically insightful framework for studying turbulence in the atmosphere. Unlike full-physics models, which must account for complex interactions between topography and moisture, idealized setups allow for targeted investigation of fundamental turbulent processes under controlled conditions [Elsherif and Taha, 2025].

This clarity is particularly valuable when analyzing small-scale anisotropy. By removing extraneous influences, idealized LES configurations enable direct examination of how specific mechanisms—such as buoyant convection or mean shear—affect turbulence generation, evolution, and dissipation. They also allow for systematic variation of parameters like stratification strength or surface forcing, making it possible to isolate causal relationships [Lefauve and Linden, 2022].

Idealized simulations provide a controlled framework for investigating turbulence mechanisms in the absence of complicating real-world factors such as topography, moisture, and large-scale weather systems [Elsherif and Taha, 2025]. This clarity is particularly useful when diagnosing isotropy, where confounding influences can obscure the interpretation of dissipation-based diagnostics.

In this study, idealized regimes are selected to activate distinct turbulence-producing dynamics in a numerically tractable and interpretable setting. These cases form a consistent foundation for assessing isotropy using dissipation-based diagnostics, providing cross-comparable results across flow types and model resolutions. Four idealized flow regimes, shown in Table 2.2, are designed to isolate specific turbulence-generating mechanisms: (1) a convective boundary layer (CBL) driven by uniform surface heating, (2) a localized thermal plume resulting from a spatially confined surface heat source, (3) a bubble perturbation shear-driven stratified layer using a hyperbolic tangent velocity profile, and (4) a random perturbation stratified shear flow, same as test case 3. Each case activates different energy injection processes—buoyancy, shear, or random perturbation to initial conditions, within a numerically stable, interpretable domain. These simplified regimes are not intended to replicate specific meteorological events but to distil fundamental turbulence behaviours relevant to boundary-layer flows.

The ability to control forcing and boundary conditions is key to ensuring repeatability and diagnostic clarity. For example, open lateral boundaries allow free development of buoyant thermals in convective cases, while periodic boundaries support sustained turbulence in shear-dominated regimes. Parameters such as stratification strength, surface forcing, or shear intensity are precisely prescribed to ensure consistency across simulations. These configurations provide a testbed for analyzing dissipation anisotropy across different regimes. Because turbulence in each case evolves from a dominant, well-characterized mechanism, the results offer interpretable comparisons in isotropic behaviour.

1.5 Dissipation Matrix and Isotropy Diagnostics

In turbulent flows, kinetic energy injected at large scales undergoes a cascade through progressively smaller eddies until it is ultimately dissipated by molecular viscosity at the smallest scales. This process is formally quantified by the viscous dissipation rate per unit mass, denoted by ϵ, which represents the irreversible conversion of kinetic energy into internal energy. The strain rate tensor captures the rate at which fluid elements deform without change in volume, and it plays a central role in energy transfer within the turbulent cascade. Physically, s_{ij} measures the local velocity gradients that are responsible for

stretching and distorting eddies, processes that enhance inter-scale interactions and contribute to the dissipation of energy at small scales [Pope, 2000]. Dissipation is inherently a small-scale phenomenon, and in the classical picture of turbulence, there is negligible dissipation in the inertial range. This assumption underpins many theoretical models and closure approaches, including Kolmogorov's 1941 theory [Kolmogorov, 1941]. However, the validity of this assumption depends critically on the flow regime and the degree to which small-scale motions have decoupled from larger-scale anisotropies imposed by shear, stratification, or boundary effects. Hence, examining dissipation structure, and the associated strain provides a sensitive insight into the degree of anisotropy present in a turbulent field. To quantify how closely a given flow conforms to these ideal conditions, a scalar diagnostic can be introduced that summarizes the deviations of the dissipation tensor from its isotropic form. This diagnostic provides a single value that captures the extent of directional imbalance in the dissipation process: lower values indicate near-isotropic conditions, while higher values point to significant anisotropy. It offers a compact and interpretable measure of small-scale structure without the need to inspect each tensor component individually [Lang and Waite, 2019]. In this study, the scalar diagnostic is adapted for use with spatially varying eddy viscosity fields, as implemented in the LES model. While the theoretical reference values assume constant viscosity, the diagnostic framework remains valid when adjusted to account for the effective viscosity at each grid point. This allows for a more realistic and meaningful interpretation of anisotropy in simulated atmospheric turbulence, especially under varying flow regimes and stratification conditions .

The diagnostic framework for assessing dissipation anisotropy traditionally assumes a constant molecular viscosity, as is common in theoretical and DNS studies. However, in practical applications such as LES, this assumption is no longer valid. LES models rely on a SGS viscosity that evolves dynamically based on local flow conditions, making the dissipation field inherently spatially and temporally variable.

To apply dissipation-based isotropy diagnostics in such settings, the formulation must be adapted to account for the eddy viscosity field used by the LES. Rather than relying on a fixed viscosity value, the modified approach computes the dissipation tensor using the effective viscosity at each grid point. This adjustment preserves the structure of the original diagnostic while extending its applicability to turbulent flows that are partially resolved and subject to modelled dissipation.

This modification is particularly important in stratified or shear-driven atmospheric flows, where the magnitude and orientation of turbulence can vary significantly across space and time. By incorporating the spatially resolved eddy viscosity, the diagnostic becomes sensitive to local anisotropy in the dissipation process without being biased by subgrid-scale model assumptions. It also allows for consistent comparison between simulations with

different resolutions or SGS parameterizations.

While this approach introduces additional complexity in the implementation, it is essential for ensuring that anisotropy assessments reflect the physical dynamics of the flow rather than artifacts of the modelling framework. In this study, the adapted diagnostic is used to evaluate the isotropy of dissipation across a range of turbulence regimes simulated with WRF-LES, enabling meaningful interpretation even under strongly inhomogeneous and anisotropic forcing conditions.

1.6 Objectives

The main goal of this thesis is to understand how turbulence develops and becomes isotropic under different types of forcing. We study this by running four different simulations using the WRF model in idealized mode. Two of the cases are driven by buoyancy, and the other two are driven by shear. We want to see how turbulence starts, how long it lasts, and how isotropic it becomes over time in each case. To do this, we measure quantities like dissipation, vorticity, and anisotropy. We also check how the results change when we increase the resolution of the simulation. By comparing these four setups, we hope to learn what controls the isotropy of turbulence and how different physical processes shape its behaviour. This can help us understand real-world atmospheric flows more clearly.

Chapter 2

Methodology

2.1 Overview

This study is carried out to explore the isotropy of atmospheric turbulence through the high-resolution simulations performed with the WRF model in LES mode. The analysis aims at estimating isotropy through dissipation-based diagnostics in four different turbulence-generating setups: a canonical CBL, a localized thermal plume, a stratified shear layer perturbed by a localized bubble, and a stratified shear layer with a homogeneous random perturbation. Each simulation was carried out in idealized mode, using the WRF.v4.3.3 model, on the Cedar cluster (Digital Research Alliance of Canada).

2.2 WRF Model and Computational Framework

The WRF model is a widely adopted, community-driven atmospheric model designed for both research and operational forecasting applications. It integrates the fully compressible, non-hydrostatic Euler equations in flux form. Additionally, it includes parametrization of various physical processes, e.g. sub-grid turbulence, surface fluxes, moist physics, radiative transfer, which enables the simulation of atmospheric processes across a broad range of spatial and temporal scales, from mesoscale dynamics to boundary layer turbulence. While the model retains the full compressibility of the governing equations, the numerical schemes used in WRF are specifically designed to dampen acoustic modes. This design allows for stable and efficient time integration without the need to resolve sound waves, which are typically not relevant in atmospheric simulations.

2.2.1 Vertical Coordinate System

WRF employs a terrain-following, hydrostatic-pressure-based vertical coordinate η, defined as:

$$\eta = \frac{p_d - p_{dt}}{p_{ds} - p_{dt}}, \tag{2.1}$$

where p_d is the dry hydrostatic pressure, p_{ds} is the surface pressure, and p_{dt} is the pressure at the model top. Near the ground, the grid follows terrain elevation, while at higher levels it transitions to constant pressure surfaces. The vertical mass metric is given by the dry air mass per unit area in each grid layer:

$$\mu_d = \frac{\partial p_d}{\partial \eta} = p_{ds} - p_{dt}. \tag{2.2}$$

This metric appears in the governing equations and controls the vertical distribution of mass and pressure. It is also used in the definition of flux-form equations and in calculating tendencies associated with vertical motion [Skamarock et al., 2019]. Our simulations have a flat bottom, which simplifies the vertical coordinate.

2.2.2 Governing Equations

The governing equations solved by WRF are the compressible Euler equations written in flux form with vertical coordinate (2.1), along with physical parameterizations. They correspond to the conservation of mass, Newton's second law, conservation of energy, and conservation of various scalars. The momentum equations in the x, y, and z directions account for pressure gradient forces and other physical forcings. The system also includes thermodynamic, continuity, scalar transport, and geopotential tendency equations. The prognostic variables include the three-dimensional mass weighted wind components $(U, V, W) = \mu_d(u, v, w)$, where the lower cases are the velocities, the potential temperature Θ and the geopotential height $\phi = gz$. Potential Temperature (θ) is the temperature that a parcel of dry air would have if it were brought adiabatically (i.e., without heat exchange) to a standard reference pressure, typically 1000 hPa. It is a conserved quantity in dry adiabatic processes and is commonly used to identify stability and mixing in the atmosphere. It is worth mentioning in these simulations that the Mach number is considered very small.

$$\theta = T \left(\frac{p_0}{p} \right)^{\frac{R_d}{c_p}}, \tag{2.3}$$

where T is the actual temperature (K), p is the ambient pressure (hPa), p_0 is the reference pressure (usually 1000 hPa), R_d is the gas constant for dry air, c_p is the specific heat capacity at constant pressure for dry air. It is important to note that although the vertical coordinate is η, the vertical velocity component w is expressed in Cartesian coordinates. The momentum equations are:

$$\frac{\partial U}{\partial t} + \nabla \cdot (\mathbf{V}u) + \mu_d \alpha \frac{\partial p}{\partial x} + \left(\frac{\alpha}{\alpha_d}\right) \frac{\partial p}{\partial \eta} \frac{\partial \phi}{\partial x} = F_U, \tag{2.4}$$

$$\frac{\partial V}{\partial t} + \nabla \cdot (\mathbf{V}v) + \mu_d \alpha \frac{\partial p}{\partial y} + \left(\frac{\alpha}{\alpha_d}\right) \frac{\partial p}{\partial \eta} \frac{\partial \phi}{\partial y} = F_V, \tag{2.5}$$

$$\frac{\partial W}{\partial t} + \nabla \cdot (\mathbf{V}w) - g\left(\left(\frac{\alpha}{\alpha_d}\right) \frac{\partial p}{\partial \eta} - \mu_d\right) = F_W. \tag{2.6}$$

In these equations, α_d is the inverse density of dry air ($1/\rho_d$), and α is the inverse density taking into account the full parcel density, $\alpha = \alpha_d(1 + q_v + q_c + q_r + q_i + \dots)^{-1}$, where q_* are the mixing ratios for water vapour, cloud, rain, ice etc. The thermodynamic and continuity equations are:

$$\frac{\partial \Theta_m}{\partial t} + \nabla \cdot (\mathbf{V}\theta_m) = F_{\Theta_m}, \tag{2.7}$$

$$\frac{\partial \mu_d}{\partial t} + \nabla \cdot \mathbf{V} = 0. \tag{2.8}$$

This form of continuity equation uses a special gradient format, which is defined below. In these equations, the subscripts x, y, and η denote differentiation,

$$\nabla \cdot \mathbf{V}a = \partial_x(Ua) + \partial_y(Va) + \partial_\eta(\Omega a),$$

and

$$\mathbf{V} \cdot \nabla a = U\partial_x a + V\partial_y a + \Omega\partial_\eta a,$$

where a represents a generic variable, and $\Omega = \dot{\eta}$ is the vertical velocity associated with the η coordinate.. The right-hand-side (RHS) terms F_U, F_V, F_W, F_{Θ_m} represent forcing terms arising from model physics, turbulent mixing, spherical projections, and the Earth's rotation. Also, $\theta_m = \theta(1 + (\frac{R_v}{R_d})q_d) \approx \theta(1 + 1.61q_v)$ The geopotential tendency equation is:

$$\frac{\partial \phi}{\partial t} + \mu_d^{-1} (\mathbf{V} \cdot \nabla\phi - gW) = 0. \tag{2.9}$$

Scalar transport for moisture and other tracers is given by:

$$\frac{\partial Q_m}{\partial t} + \nabla \cdot (\mathbf{V} q_m) = F_{Q_m}, \tag{2.10}$$

where $Q_* = \mu_d q_*$. The hydrostatic relation is:

$$\frac{\partial \phi}{\partial \eta} = -\alpha_d \mu_d, \tag{2.11}$$

The equation of state for pressure is:

$$p = p_0 \left(\frac{R_d \theta_m}{p_0 \alpha_d} \right)^{\gamma}, \tag{2.12}$$

where $\gamma = c_p / c_v$.

The WRF model integrates the atmospheric equations using a time-split third-order Runge–Kutta scheme. Horizontal advection is computed using a fifth-order scheme, while vertical advection uses a third-order scheme. These high-order methods help accurately capture sharp gradients and turbulent structures. The higher-order horizontal scheme reduces numerical diffusion across the larger horizontal domain, while the lower-order vertical scheme helps maintain stability given the finer vertical resolution and strong stratification.

LES resolves large-scale turbulent motions directly, while SGS effects are modelled. In Cartesian coordinates, the filtered momentum equation takes the form:

$$\frac{\partial \bar{u}_i}{\partial t} + \bar{u}_j \frac{\partial \bar{u}_i}{\partial x_j} = -\frac{1}{\rho} \frac{\partial \bar{p}}{\partial x_i} + \nu \frac{\partial^2 \bar{u}_i}{\partial x_j^2} - \frac{\partial \tau_{ij}}{\partial x_j}, \tag{2.13}$$

where $\bar{u}_i$ is the resolved velocity, $\tau_{ij} = \overline{u_i u_j} - \bar{u}_i \bar{u}_j$ is the subgrid stress tensor, and ν is the molecular viscosity. WRF incorporates the τ_{ij} term in WRF coordinates into the F_U,F_V, and F_W forcing terms. The eddy viscosity ν_t is computed from the subgrid turbulence kinetic energy (TKE) as:

$$\nu_t = c_k l \sqrt{k}, \tag{2.14}$$

where k is the subgrid TKE, l is the mixing length (typically related to grid spacing), and c_k is a model constant. The subgrid stress tensor is then modelled using:

$$\tau_{ij} - \frac{1}{3} \delta_{ij} \tau_{kk} = -2 \nu_t \bar{s}_{ij}, \tag{2.15}$$

where $\bar{S}_{ij}$ is the resolved strain rate matrix:

$$\bar{s}_{ij} = \frac{1}{2}\left(\frac{\partial \bar{u}_i}{\partial x_j} + \frac{\partial \bar{u}_j}{\partial x_i}\right). \tag{2.16}$$

The model uses modular physics packages, meaning that physical processes such as microphysics, radiation, and boundary-layer dynamics are implemented as independent components that can be activated or replaced as needed. It is parallelized using MPI for efficient performance on high-performance computing systems. All simulations were run on the Cedar cluster provided by Compute Canada, and outputs were saved in NetCDF format for compatibility with standard analysis tools such as WRF-Python.

2.2.3 Richardson Number and Stability Criteria

The gradient Richardson number (Ri) is a nondimensional quantity that characterizes the balance between stratification (buoyancy) and vertical shear in a stably stratified flow. It is defined as:

$$Ri = \frac{g}{\theta}\frac{\partial\theta/\partial z}{(\partial u/\partial z)^2 + (\partial v/\partial z)^2}, \tag{2.17}$$

where g is the gravitational acceleration, θ is the potential temperature, $\partial\theta/\partial z$ is the vertical potential temperature gradient, and $\partial u/\partial z$ and $\partial v/\partial z$ are the vertical gradients of the horizontal velocity components [Miles, 1961].

The Richardson number measures the competition between stabilizing buoyancy effects (numerator) and destabilizing vertical shear (denominator). It plays a key role in predicting whether turbulence will be generated or suppressed in stratified shear flows. A classical result in geophysical fluid dynamics is that when $Ri < 0.25$, the flow may become dynamically unstable and is prone to shear-driven instabilities such as Kelvin–Helmholtz instability. This value is often referred to as the critical Richardson number. When $Ri > 0.25$, stratification is sufficiently strong to suppress turbulence generation by vertical shear, and the flow tends to remain laminar [Howard, 1961].

2.3 Domain Setup, Resolution, and Initialization

In this study, four idealized turbulence scenarios were simulated using the WRF-LES model: a CBL, plume, localized bubble-perturbed stratified shear flow, and randomly

perturbed stratified shear flow. Each case represents a distinct turbulence generation mechanism, and its initial thermodynamic and dynamic conditions were configured accordingly.

Table 2.1: Simulation configurations for each idealized case at low and high resolution.

Simulation Case	**Resolution**	**Length (km)**	**Height (km)**	Δx **(m)**	Δz **(m)**
CBL	Low	12	2	50	42
CBL	High	12	2	25	21
Plume	Low	12	10	50	42
Plume	High	12	10	25	21
Bubble Shear Flow	Low	12	10	50	42
Bubble Shear Flow	High	12	10	25	21
Randomly Shear Flow	Low	12	10	50	42
Randomly Shear Flow	High	12	10	25	21

The CBL and Plume simulations employed an initially layered potential temperature profile with zero initial velocity. The initial potential temperature increases steadily with height, showing that the air becomes progressively more stable as we move upward. Near the surface, the gradient is small, suggesting a well-mixed layer, while the sharper increase aloft indicates a stable cap that limits vertical mixing. The CBL was driven by uniform surface heating, while the Plume case included a localized circular heat source. The Plume case uses open boundary conditions, which allow fluid to enter or leave the domain, minimizing artificial wave reflections at the boundaries, and the CBL uses a periodic boundary condition due to the horizontal homogeneity of the heat flux. In the CBL case, the Ozmidov scale is about 20 meters, which shows the smallest size where buoyancy still affects the flow. In the plume case, the spatial distribution of the surface heat flux $q(x, y)$ is defined by the following equation:

$$q(x,y) = \begin{cases} q_{max} \cos^2\left(\frac{\pi}{2} \frac{\sqrt{(x-x_0)^2+(y-y_0)^2}}{R}\right), & \text{if } \sqrt{(x-x_0)^2+(y-y_0)^2} \leq R, \\ 0, & \text{if } \sqrt{(x-x_0)^2+(y-y_0)^2} > R, \end{cases} \tag{2.18}$$

where $q_{max} = 0.24$ K m/s denotes the maximum heat flux, $R = 2000$ m is the radius of the heat source, and (x_0, y_0) represents the coordinates of the center of the heat source at the ground surface at the center of the domain. In the CBL case, the heat flux is uniform across the entire surface: $q(x, y) = q_{max}$.

The Shear-Driven simulations were initialized with a hyperbolic tangent profile for both potential temperature and velocity. The initial stratification and velocity profiles of the shear-driven and randomly perturbed test cases were configured based on a target Richardson number profile. This ensured that the initial flow resides near the marginal stability condition, allowing the development of turbulence from shear instability without requiring external forcing. The initial velocity profile was given by:

$$U(z) = \frac{\Delta U}{2} \tanh\left(\frac{z - z_0}{d_{\text{shear}}}\right), \tag{2.19}$$

where ΔU is the difference in velocity across the shear layer, d_{shear} is the thickness of the shear transition, and $z_0 = 5000$ m. The initial potential temperature was given by:

$$\theta(z) = \theta_0 + \frac{\Delta\theta}{2} + \frac{\Delta\theta}{2} \tanh\left(\frac{z - z_0}{d_{\text{shear}}}\right), \tag{2.20}$$

where $\Delta\theta$ is the potential temperature difference across the shear layer, therefore U and θ have the same tickness. The initial potential temperature and velocity profiles were set so that the minimum Richardson number in the domain was 0.3 for the bubble perturbed shear case, which is slightly above the critical value for shear instability. For the randomly perturbed shear simulation, the minimum Ri number was considered 0.1 to ensure the creation of the shear instability.

To trigger turbulence, a perturbation was added to the initial condition. Two perturbations were considered: a spatially localized bubble and random perturbations. In the bubble case, the local Richardson number was reduced below the critical threshold and created a small region of instability, allowing turbulence to develop in a controlled area of the domain. The potential temperature field of the bubble is given by:

$$\Delta\theta(x, y, z) = \begin{cases} -\Delta \sin\left(\frac{\pi}{2} \frac{z}{d_{\text{shear}}}\right) \times \cos^2\left(\frac{\pi}{2}\sqrt{\left(\frac{x}{d_{\text{x}}}\right)^2 + \left(\frac{y}{d_{\text{y}}}\right)^2}\right), & \text{if } |\frac{z-z_0}{d_{shear}}| \leq 1, \\ 0, & \text{if } |\frac{z-z_0}{d_{shear}}| > 1. \end{cases} \tag{2.21}$$

where Δ is the magnitude of the perturbation of the temperature, d_x and d_y are the length of the bubble in the x and y direction. In this case $d_x = d_y = 2500$m.

For the next test case, the random perturbations were added instead of the warm bubble throughout the domain. After that, the geopotential and density fields were recomputed to restore hydrostatic balance in both shear cases. These simulations used periodic boundary

conditions, allowing fields exiting one boundary to re-enter from the opposite side, thereby mimicking infinite or homogeneous domains without boundary-induced effects.

To assess resolution effects, each scenario was simulated at two resolutions: a low-resolution setup with a 50 m horizontal grid spacing and 240 vertical levels, assuming approximately uniform spacing with $\Delta z \approx 42$m, and a high-resolution setup with 25 m horizontal spacing and 480 vertical levels, with a vertical spacing of 21 m. The output intervals were configured to resolve the temporal evolution of the turbulent structures and the energy dissipation metrics.

Table 2.2: Simulation setup and initial conditions for each case.

Attribute	**CBL**	**Plume**	**Bubble Shear**	**Random shear**
Potential Temperature	Layered structure	Layered structure	tanh	tanh
Initial Velocity	Zero	Zero	tanh	tanh
Boundary Conditions	Periodic	Open	Periodic	Periodic
Forcing Mechanism	Uniform surface heating	Localized heat source	Shear instability + localized bubble perturbation	shear instability + random perturbation

Figure 2.1 shows the initial potential temperature profiles used for the different idealized simulations. In the CBL case, the temperature increases slowly with height up to about 2 km. The plume case includes a background temperature gradient with a localized warm bubble around 5 km. The bubble shear and randomly perturbed shear cases have the same overall profile, featuring a smooth transition near 5 km using a tanh shape.

Figure 2.2 shows the initial horizontal velocity profiles in the x-direction. Both the CBL and plume cases have zero background flow, while the shear cases include a smooth velocity increase with height. This shear is centred around 5 km and introduces velocity gradients that will drive shear-driven turbulence in the simulations.

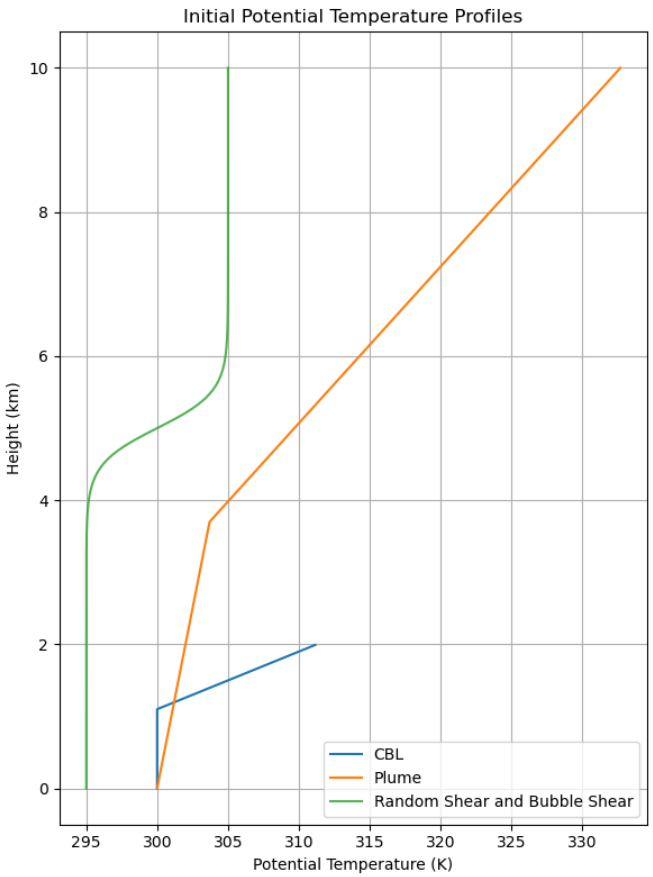


Figure 2.1: Initial potential temperature profiles for each simulation. The CBL profile is 2 km. The plume case includes a warm anomaly at 5 km. Both bubble shear and random shear share the same tanh-shaped profile.

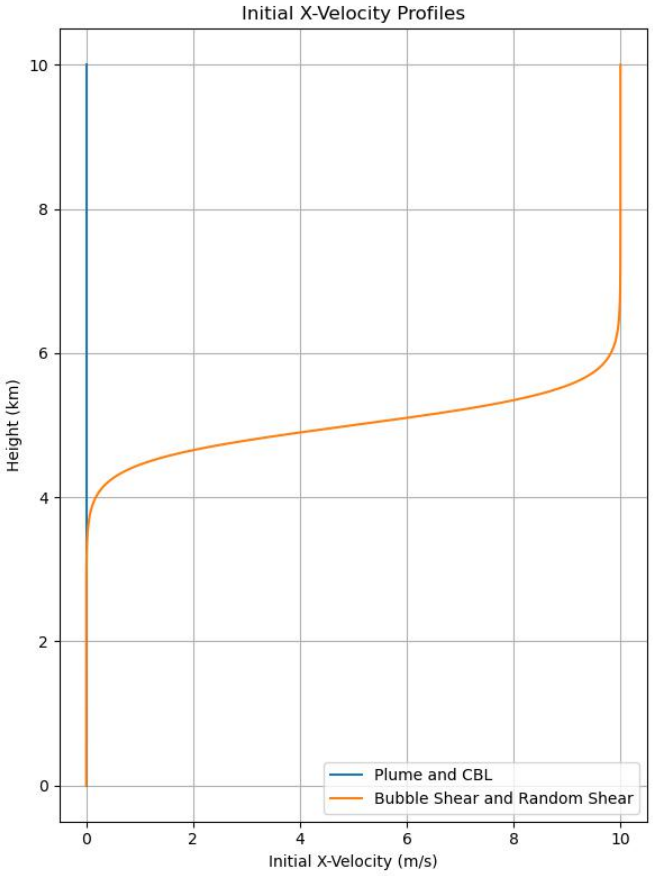


Figure 2.2: Initial horizontal (x-direction) velocity profiles. The CBL and plume cases start from rest, while the shear cases have a tanh profile centred near 5 km to induce shear.

2.4 Physical Settings

All simulations were performed in dry, idealized mode to focus on the intrinsic dynamics of turbulence without the influence of moist processes. Most physical parameterization schemes, including microphysics, radiation, cumulus convection, and planetary boundary layer (PBL) parameterizations, were turned off; however, surface scheme and subgrid turbulence schemes were used. Surface heat fluxes were prescribed in the CBL and plume cases, and no surface heat flux in the shear cases. Surface momentum fluxes were computed using a surface layer scheme. Subgrid-scale turbulence was modelled using a prognostic eddy viscosity formulation with isotropic mixing as described above. Acoustic time-splitting and divergence damping techniques were used to maintain stability during the integration of the compressible equations [Wicker and Skamarock, 2002].

2.5 Isotropy Diagnostics

2.5.1 Dissipation Ratios in Isotropic Turbulence (Taylor's Ratios)

In this section, we do *not* use Einstein's summation convention. All summations are written explicitly to avoid confusion. In incompressible turbulence, the molecular dissipation rate per unit mass is given by:

$$\epsilon = 2\nu \sum_{i,j} \langle s_{ij} s_{ij} \rangle, \tag{2.22}$$

where ν is the molecular viscosity, s_{ij} is the strain-rate tensor, and $\langle \cdot \rangle$ denotes a domain average.

Taylor [1935] and subsequent work Pope [2000] show that under statistical isotropy, the normalized dissipation matrix

$$D_{ij} = \frac{\langle s_{ij}^2 \rangle}{\sum_{m,n} \langle s_{mn} s_{mn} \rangle} \tag{2.23}$$

must be invariant under coordinate rotations. This implies that all diagonal elements are equal and all off-diagonal elements are also equal.

Diagonal Terms

For incompressible flow,

$$\sum_i \frac{\partial u_i}{\partial x_i} = 0. \tag{2.24}$$

This constraint reduces the degrees of freedom in the diagonal strain components. Under isotropy, one obtains [Taylor, 1935]:

$$\langle s_{ii} s_{ii} \rangle = \frac{2}{15} \sum_{m,n} \langle s_{mn} s_{mn} \rangle, \tag{2.25}$$

so that:

$$\frac{\varepsilon_{ii}}{\varepsilon_{\text{tot}}} = \frac{2}{15}. \tag{2.26}$$

Off-Diagonal Terms

For off-diagonal components ($i \neq j$):

$$\langle s_{ij} s_{ij} \rangle = \frac{1}{4} \left[\left\langle \left(\frac{\partial u_i}{\partial x_j} \right)^2 \right\rangle + \left\langle \left(\frac{\partial u_j}{\partial x_i} \right)^2 \right\rangle + 2 \left\langle \frac{\partial u_i}{\partial x_j} \frac{\partial u_j}{\partial x_i} \right\rangle \right]. \tag{2.27}$$

Under isotropy, the cross term vanishes and the remaining terms are equal [Taylor, 1935]:

$$\langle s_{ij} s_{ij} \rangle = \frac{1}{2} \left\langle \left(\frac{\partial u_i}{\partial x_j} \right)^2 \right\rangle = \frac{1}{10} \sum_{m,n} \langle s_{mn} s_{mn} \rangle, \tag{2.28}$$

so that:

$$\frac{\varepsilon_{ij}}{\varepsilon_{\text{tot}}} = \frac{1}{10}, \quad i \neq j. \tag{2.29}$$

As a result, for molecular dissipation in isotropic turbulence, the normalized dissipation matrix D_{ij} is equal to 2/15 on the diagonal and 1/10 on the off-diagonal.

2.5.2 Extension to LES with Eddy Viscosity

Lang and Waite [2019] showed that sub-filter dissipation in filtered DNS obeys Taylor's ratios under isotropic turbulence. In LES, the eddy dissipation is a parameterization of this

sub-filter dissipation, and so it should behave similarly. In our LES model, the effective eddy viscosity K varies spatially and temporally. To account for this, we apply the same theoretical framework using K at each grid point.

The rate of SGS dissipation per unit mass is defined as:

$$\epsilon = 2 \sum_{i,j} \langle K s_{ij} s_{ij} \rangle, \tag{2.30}$$

where s_{ij} is the resolved strain-rate tensor. The normalized contribution of each component is:

$$\epsilon_{ij} = \frac{2\langle K s_{ij} s_{ij} \rangle}{\epsilon}. \tag{2.31}$$

We assess isotropy by comparing ϵ_{ij} against theoretical ratios:

$$S_{ij}^{\text{theo}} = \begin{cases} \frac{2}{15}, & i = j, \\ \frac{1}{10}, & i \neq j. \end{cases} \tag{2.32}$$

To quantify deviations from isotropy, similar to Lang and Waite [2019], we define:

$$\chi_\epsilon = \frac{1}{6} \sum_{i,j} \left(\frac{\epsilon_{ij}}{\epsilon} - S_{ij}^{\text{theo}} \right)^2. \tag{2.33}$$

Small values of χ_ϵ indicate near-isotropic dissipation. We compute χ_ϵ using time-averaged values from the central horizontal domain, minimizing boundary effects and better reflecting bulk turbulence behaviour.

In summary, isotropy diagnostics use dissipation matrix components to help us understand how small-scale turbulent energy dissipation is distributed in different directions. Theoretical ratios derived from molecular viscosity are useful benchmarks, and our eddy-viscosity extension allows for application in LES. Across simulations, deviations from isotropic values are a clear indicator of anisotropy, affected by different forcing and resolution. The scalar diagnostic χ_ϵ captures these deviations and investigates the flow's isotropic behaviour.

Chapter 3

Results

3.1 Convective Boundary Layer

The CBL simulation was performed over a total duration of 6 hours to ensure the development of fully turbulent flow. This extended run time allows the turbulence to evolve from an initially quiet state with no velocity to a turbulent convective regime due to surface heating.

To visualize the evolution of CBL over time, two sets of contour plots are presented: Figure 3.1 for total vorticity and Figure 3.2 for potential temperature. The high resolution simulation was used in these figures. Figures includes four selected times: $t = 14$, 30, 60, and 240 minutes. Each time snapshot highlights how turbulent structures evolve. We begin with small convective plumes near the surface, then observe how the mixed layer and vorticity depth grow over time. These times are chosen to represent distinct regimes of flow development throughout the simulation, capturing the early transition, growth, and mature phases of turbulent convection. The vorticity contours (Figure 3.1) clearly show the gradual upward development of convective structures, with small plumes at $t = 14$ minutes growing into larger turbulent eddies by $t = 60$ minutes, and eventually reaching a deep mixed layer at $t = 240$ minutes. At $t = 14$ minutes, strong vorticity is confined below 500 m. By $t = 30$ minutes, it reaches 750 m, and extends up to 1.2 km at $t = 60$ minutes. At $t = 240$ minutes, vorticity spans almost the full domain up to 1.25 km, indicating deep turbulent mixing. In parallel, the potential temperature plots (Figure 3.2) show that at $t = 14$ minutes, we see a sharp gradient near 1 km, the initial capping inversion, with colder, well-mixed air below. As time progresses, the mixed layer thickens: the gradient shifts upward to 1.2 km at $t = 60$ minutes and 1.5 km at $t = 240$ minutes, consistent with

vertical mixing. Eventually, since there is surface heating, but no cooling or large forcing, the CBL will grow in time.

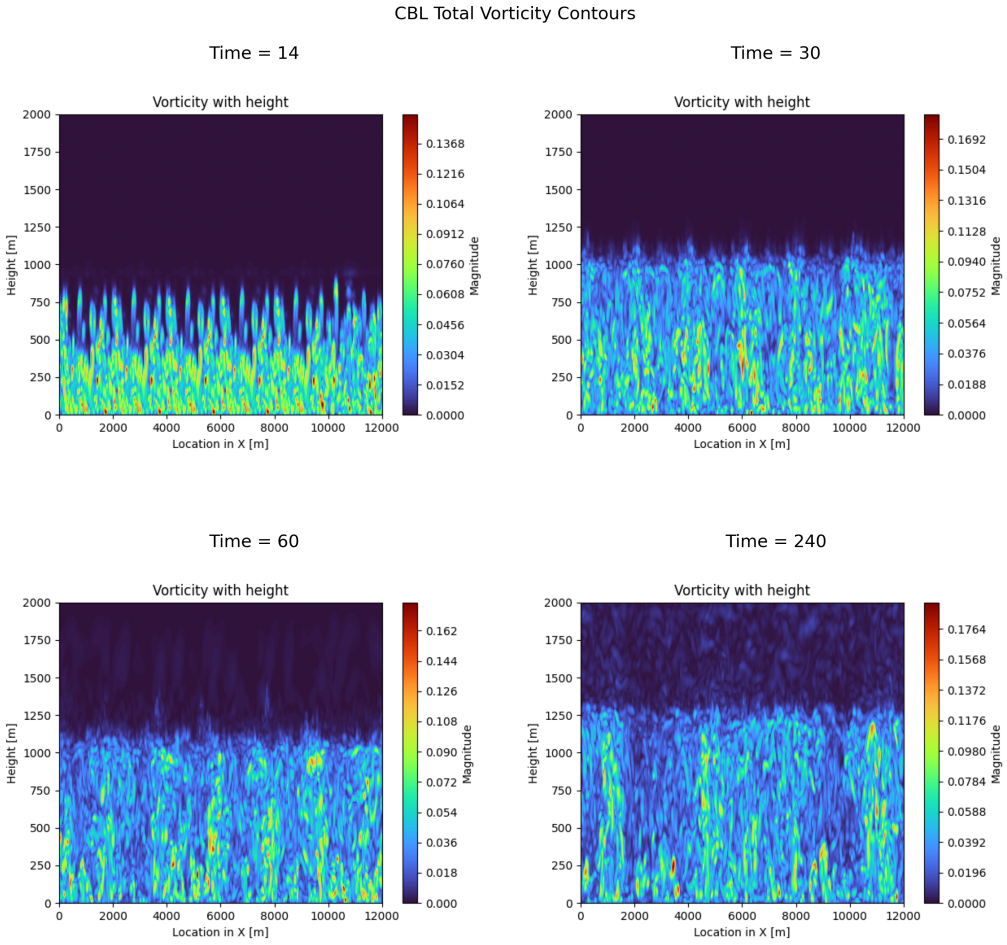


Figure 3.1: Magnitude of total vorticity contour of CBL simulation during the fully developed stage for four selected times.

For the CBL case, the Ozmidov scale is estimated using the initial potential temperature profile to compute the Brunt–Väisälä frequency N, together with a representative dissipation rate ϵ taken from the early turbulent peak. This results in an Ozmidov scale of approximately 20 m. This value represents the smallest scale at which buoyancy effects remain important in the convective boundary layer and suggests that turbulence approaches isotropy only at smaller scales.

In the CBL simulation, all dissipation values are domain-averaged over the lower half of

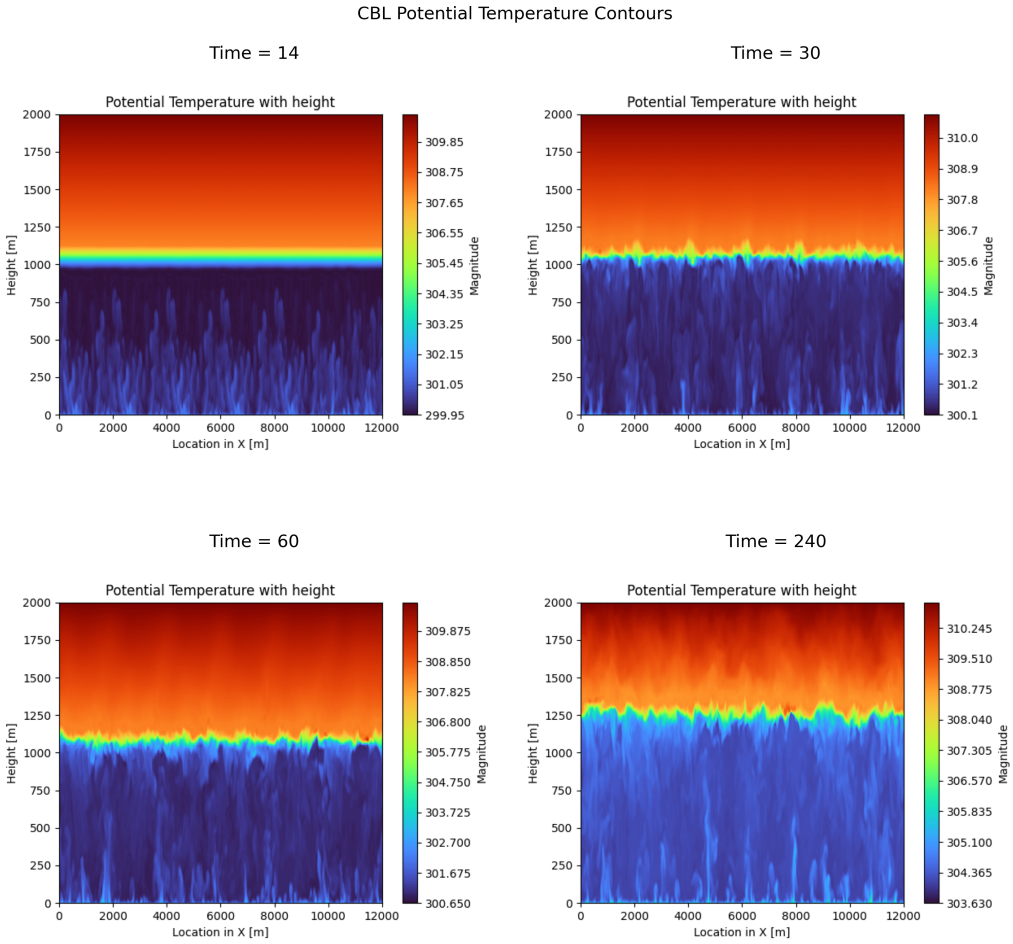


Figure 3.2: Potential Temperature contour of CBL simulation during fully developed stage for four selected times.

the domain, where turbulence is present. Figure 3.3 shows the time evolution of the domain-averaged total dissipation ε_{tot} for the high-resolution CBL simulation over the full 6-hour run. The dissipation initially increases sharply, reaching a peak around 20 minutes, which corresponds to the onset of strong convective mixing as the surface heating drives vertical motions. Following the peak, the dissipation drops and then gradually increases again, suggesting the transition toward a more developed turbulent regime. After approximately 60 minutes, the curve enters a quasi-steady phase, with dissipation values fluctuating around a slowly increasing trend. This suggests that by the 1-hour mark, turbulence is fully established and sustained by the constant surface heating. This transition to

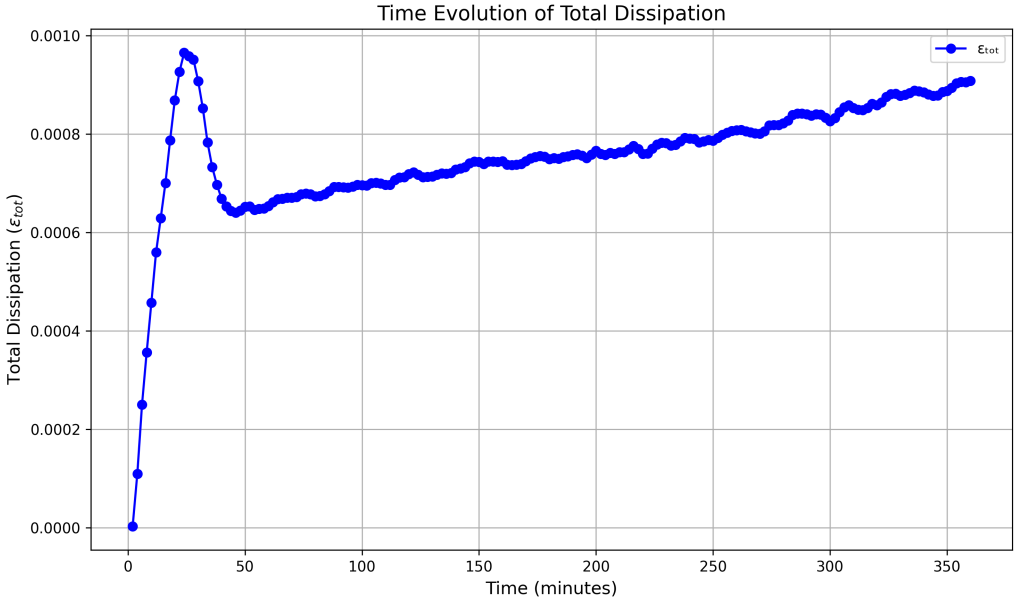


Figure 3.3: Temporal evolution of total dissipation rate in the CBL simulation.

a convective regime is also reflected in the anisotropy diagnostics and the behaviour of dissipation components. This phase is the focus of further diagnostics in the analysis.

Figure 3.4 compares the six components of the anisotropy matrix between the high-resolution and low-resolution simulations. The top subplot shows the diagonal elements (ϵ_{11}, ϵ_{22}, ϵ_{33}), while the bottom subplot presents the off-diagonal elements (ϵ_{12}, ϵ_{13}, ϵ_{23}). Theoretical isotropic values of 2/15 (diagonal) and 1/10 (off-diagonal) are plotted as horizontal reference lines.

In the diagonal components, ϵ_{33} (vertical direction) consistently shows the largest component, which is expected in buoyancy-driven turbulence where vertical motions dominate. The horizontal components ϵ_{11} and ϵ_{22} are closer to the isotropic benchmark, especially at higher resolution. Notably, all three diagonal components remain above the theoretical 2/15 value throughout the simulation, with ϵ_{33} being the most elevated, followed by ϵ_{22} and ϵ_{11}. Overall, the high-resolution simulation shows improved alignment with the theoretical 2/15 value across all components.

In the off-diagonal terms, all components remain below the theoretical 1/10 value after the first hour until the end of the simulation. Among them, ϵ_{13} and ϵ_{23} are consistently closer to the benchmark, while ϵ_{12} starts farther and gradually increases over time, indicat-

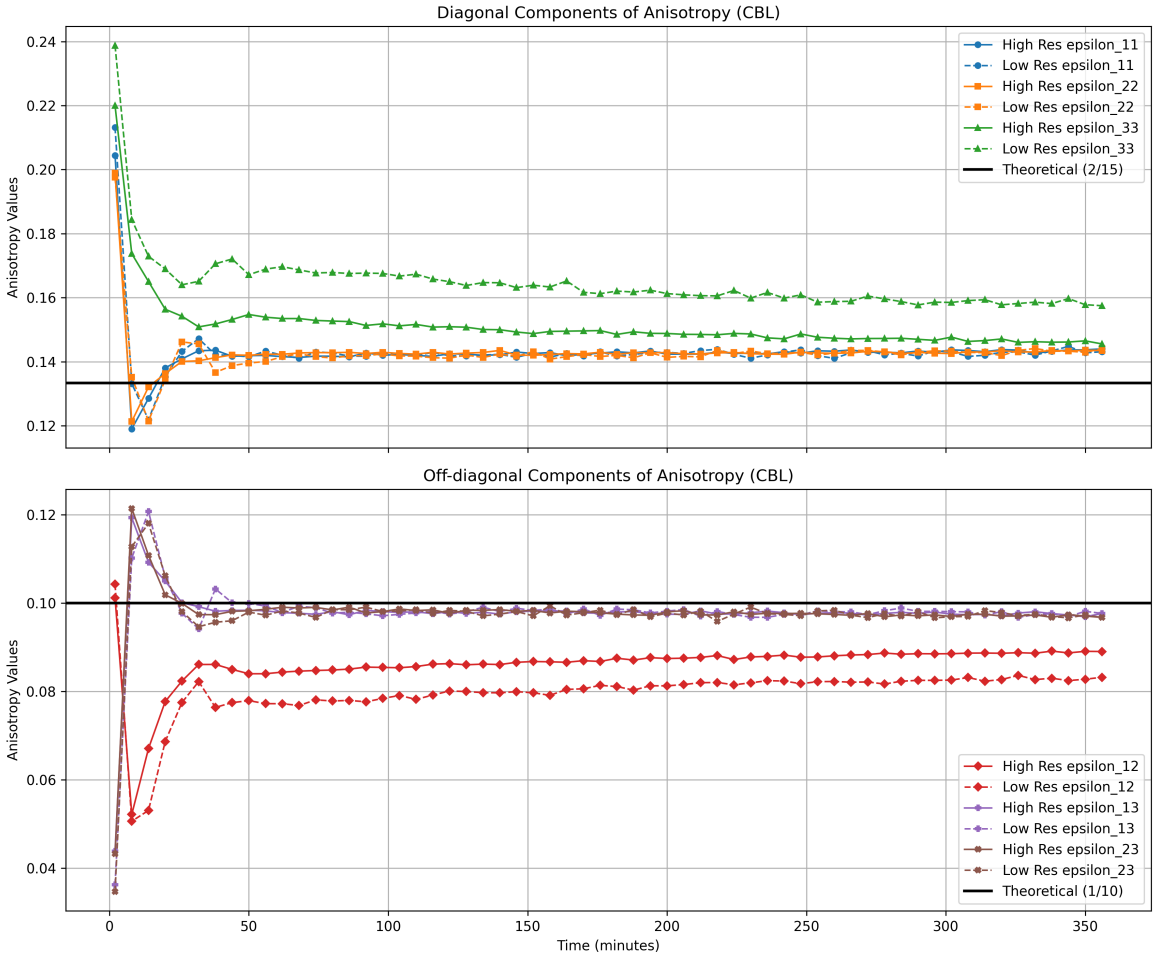


Figure 3.4: Anisotropy matrix components(ϵ_{ij}) in the CBL simulation, comparing high- and low-resolution cases. Top: diagonal elements with theoretical value 2/15. Bottom: off-diagonal elements with theoretical value 1/10.

ing slower convergence. Again, the high-resolution case more closely tracks the theoretical value, especially after the turbulence is fully developed. These results suggest that spatial resolution plays a critical role in capturing isotropic behaviour in LES, particularly in the off-diagonal shear components.

Figure 3.5 shows the evolution of the total anisotropy metric χ_ϵ over time for the CBL simulations, with both high- and low-resolution results plotted on a logarithmic scale. At the beginning of the simulation, the χ_ϵ is large due to the rapid growth of organized

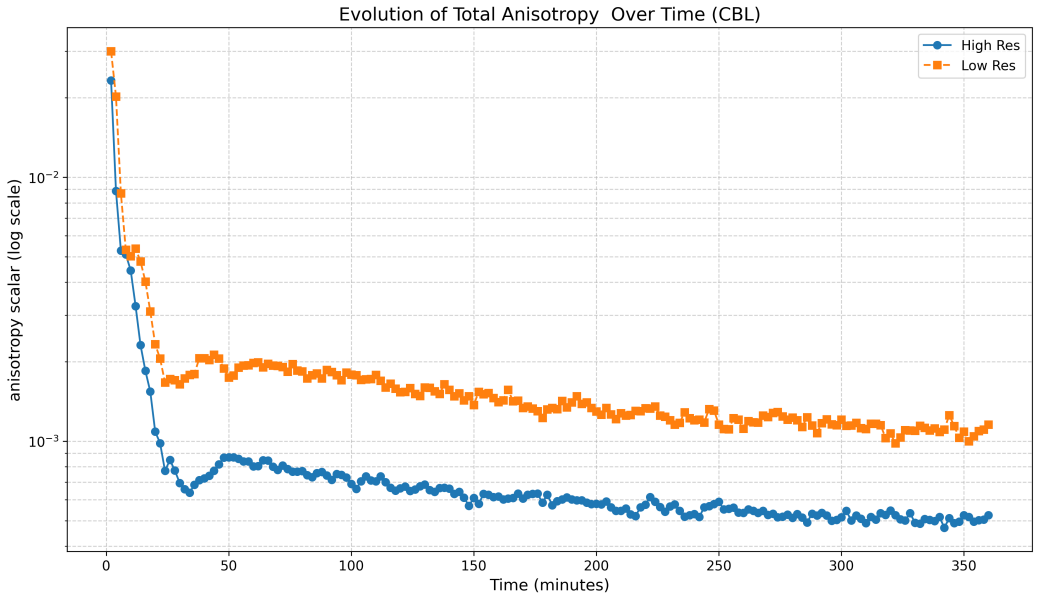


Figure 3.5: Evolution of total anisotropy χ_ϵ in log scale for high- and low-resolution CBL simulations.

convective plumes. As the turbulence develops and energy cascades to smaller scales, χ_ϵ decreases steadily, indicating a gradual transition toward a more isotropic state. After approximately one hour, the values of χ_ϵ have shorter range of changes compared to the first hour of the simulation, suggesting that the flow has entered a statistically steady turbulent regime, during which the degree of isotropy is not changing much. The high-resolution simulation maintains lower anisotropy values throughout, demonstrating that finer grid spacing allows for better representation of small-scale turbulent motions and a closer approach to isotropy. Taken together, the vorticity growth, dissipation stabilization, and anisotropy decay all consistently indicate that by the 1-hour mark, the flow achieves a statistically stationary turbulent regime where the isotropy assumptions used in LES diagnostics become more valid, especially at higher resolution.

3.2 Plume

The plume simulations were performed for a total duration of 1 hour. This time frame was chosen to capture the full development of turbulence induced by a localized surface heat source. The short duration reflects the transient nature of plume evolution and

the rapid onset of convective turbulence. Initially, at $t = 14$ minutes, a narrow core of elevated vorticity is visible extending up to about 1 km. The structure is fairly vertical and confined. This simulation is limited to 1 hour because beyond that, gravity waves and boundaries interactions affects the plume, and we are trying to avoid artifacts from lateral boundaries. To illustrate the evolution of the buoyant plume, two contour plots are presented from the high-resolution test case, where they show the first 2.5 km of the vertical domain. Figure 3.6 shows the total vorticity field at four selected times: $t = 14$, 30, 46, and 60 minutes, capturing the progressive development of the plume structure. By $t = 30$ minutes, this region of strong vorticity extends up to nearly 2 km and becomes slightly wider. The plume shows multiple small-scale eddies forming around the central updraft. At $t = 46$ minutes, vorticity remains strong and vertically aligned, reaching above 2.3 km. The structure becomes more turbulent and complex in shape, indicating enhanced mixing. At $t = 60$ minutes, the height of the strong vorticity core remains around 2.3 km, suggesting that the vertical growth has saturated, but lateral spreading is still ongoing. Figure 3.7 depicts the potential temperature field at the same time intervals. To emphasize the region of interest, only the lower 2.5 km of the domain height is shown in both plots. These visualizations highlight the plume's upward growth and spreading, which becomes fully developed by the end of the simulation. The temperature field shows a well-defined vertical plume core at $t = 14$ minutes with slight upward bending, reaching just over 1 km. By $t = 30$ minutes, the warm core has expanded and reached above 2 km. At $t = 46$ and 60 minutes, the upper tip of the temperature anomaly stays around 2.4 km, but the lateral spread increases. The sharp gradient between the rising plume and the surrounding air weakens over time, suggesting mixing. The low-level vorticity near the boundaries is growing due to initial noise.

The values in the plume simulation are averaged over a 3D box measuring 3 km in the x and y dimensions and 2.5 km in height. Figure 3.8 illustrates the time evolution of the total dissipation ϵ_{tot} for the high-resolution plume simulation. The simulation was run for 60 minutes, during which several peaks and troughs in dissipation were observed. These oscillations reflect the transient nature of the plume dynamics as the localized heat source induces strong updrafts followed by phases of decay and reorganization. The dissipation increases rapidly during the early minutes as turbulence develops, followed by a series of fluctuations that indicate ongoing energy exchanges between the buoyant forcing and the turbulent structures. The highest peaks in dissipation occur after the first 30 minutes, suggesting that the turbulence becomes fully active in the second half of the simulation. To compare the values of total dissipation in the CBL and plume cases, it was found that the CBL is higher. This can be the result of having a greater area of heat source in the CBL case, and the region of averaging in the plume contains some domains that are not

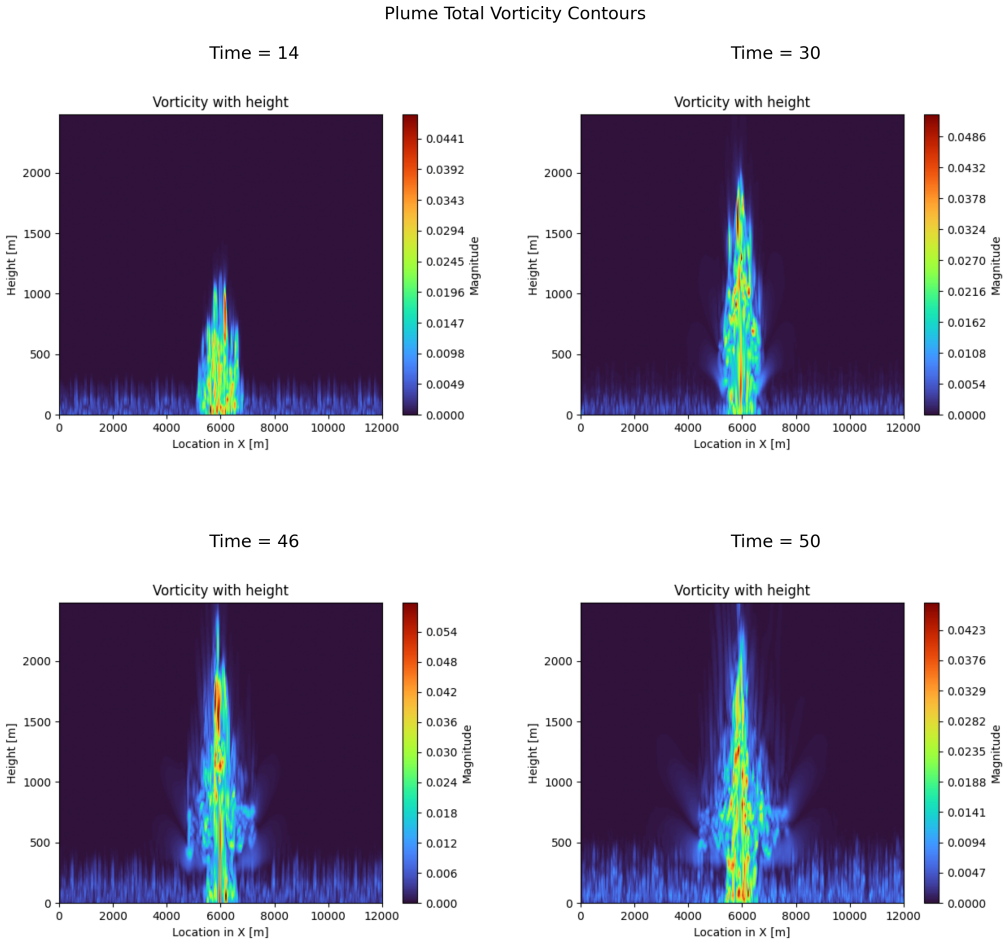


Figure 3.6: Magnitude of total vorticity contour of plume simulation during the fully developed stage for four selected times.

turbulent and have a smaller dissipation.

Figure 3.9 shows the temporal evolution of the anisotropy components for the plume simulation. The top panel presents the diagonal components ϵ_{11}, ϵ_{22}, and ϵ_{33} for both high and low resolution, compared against the isotropic benchmark value of 2/15. The bottom panel displays the off-diagonal components ϵ_{12}, ϵ_{13}, and ϵ_{23}, with the theoretical isotropic expectation of 1/10.

The diagonal components for both resolutions initially overshoot the theoretical line before gradually stabilizing, but the high-resolution curves exhibit earlier and more consistent

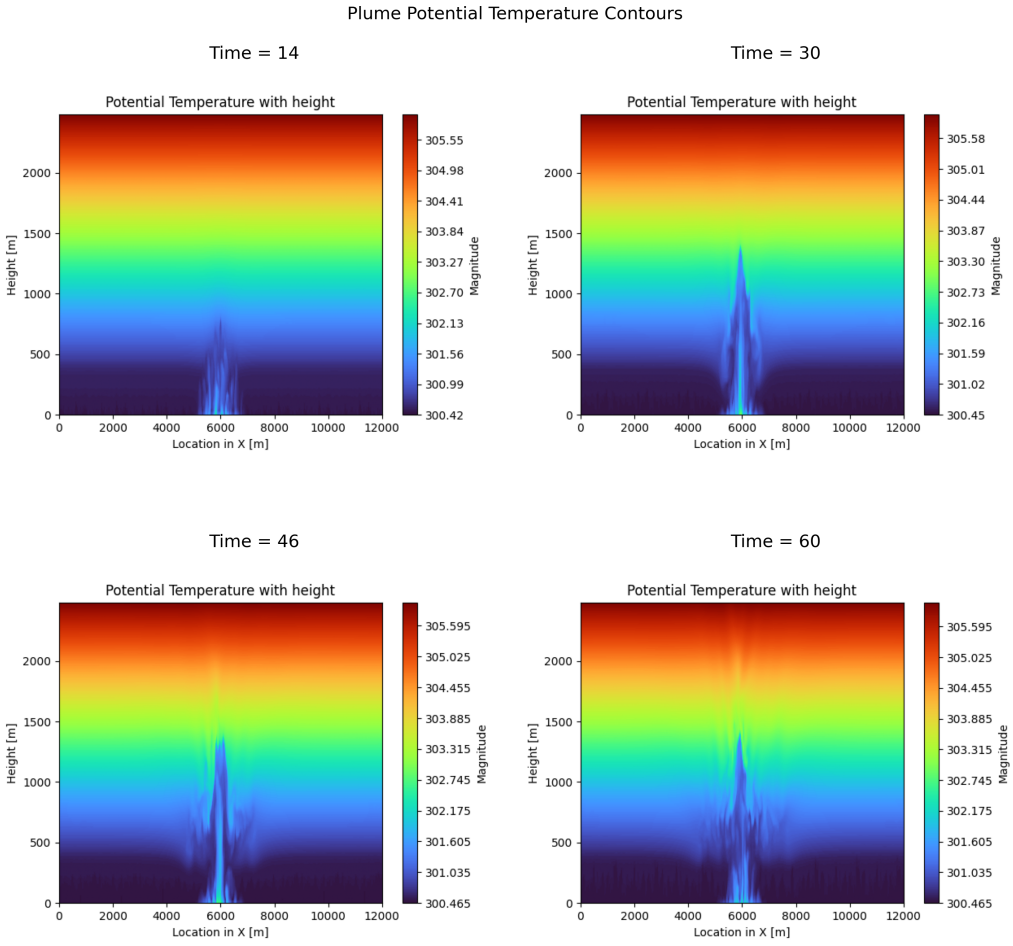


Figure 3.7: Potential Temperature contour of plume simulation during fully developed stage for four selected times.

convergence. Among them, ϵ_{33}, corresponding to the vertical direction, shows the largest component with the highest deviation from isotropy. This component also shows a clearer distinction between resolutions: the high-resolution case stabilizes closer to the isotropic line compared to the low-resolution one, which remains elevated throughout. This is expected due to the strong buoyancy-induced vertical motions in the plume case. In contrast, ϵ_{11} and ϵ_{22} (the horizontal directions) settle much closer to the isotropic limit, especially in the high-resolution simulation.

For the off-diagonal terms, ϵ_{13} and ϵ_{23} are better aligned with the theoretical 1/10 line, particularly in the high-resolution case. ϵ_{12} remains consistently lower, and the gap between

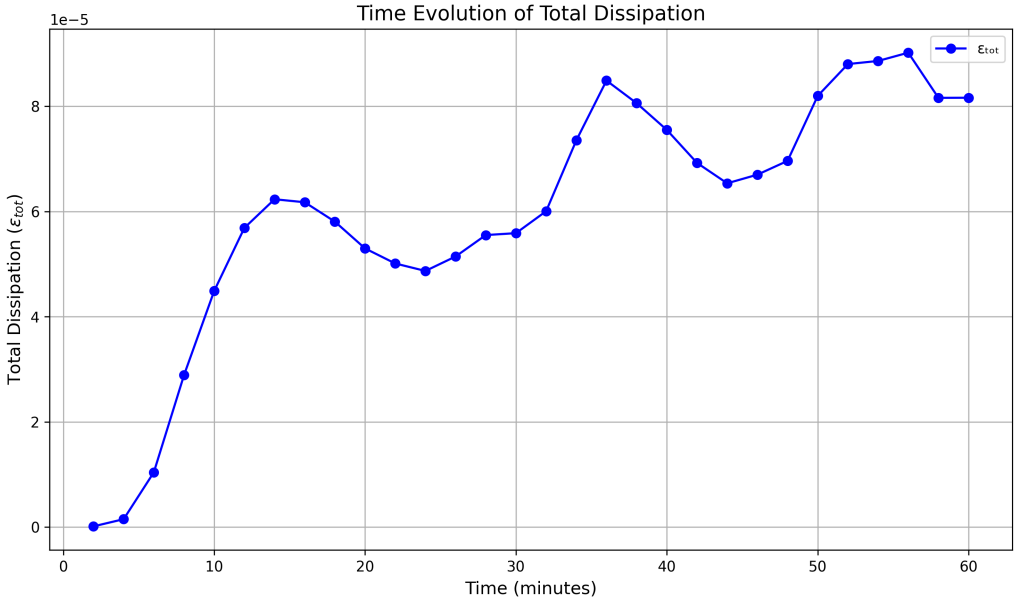


Figure 3.8: Temporal evolution of total dissipation rate in the plume simulation.

high and low resolution is more apparent here. This suggests that the plume-induced turbulence is more organized in the vertical plane (xz and yz), where the primary effect of surface heating occurs, and less so in the purely horizontal plane (xy). High-resolution simulations tend to exhibit smoother trends and converge more closely to the expected values, confirming the improved isotropy with increased resolution. This is especially evident in the off-diagonal terms, where the high-resolution case shows reduced fluctuation and more reliable adherence to isotropic expectations compared to the low-resolution run.

To compare the CBL and plume simulations, in both cases, ϵ_{11} and ϵ_{22} move toward the theoretical isotropic value of 2/15, but in the CBL simulation, they reach it more smoothly and stay close to it for the rest of the run. The vertical component ϵ_{33} is consistently larger in both cases, especially in the plume simulation, where it stays around 0.2 for most of the time. This shows stronger vertical gradients of vertical velocity caused by plume injection. For the off-diagonal terms, both simulations show convergence toward the isotropic value of 1/10, but the CBL case does this more clearly. In the plume case, ϵ_{12} remains lower than isotropic turbulence metrics, and other components fluctuate more, showing that the plume introduces more directional effects. Finally, the difference between high and low resolution is small in the CBL simulation, but more visible in the plume case, especially in ϵ_{33} and ϵ_{23}, suggesting higher sensitivity to resolution when simulating localized plumes.

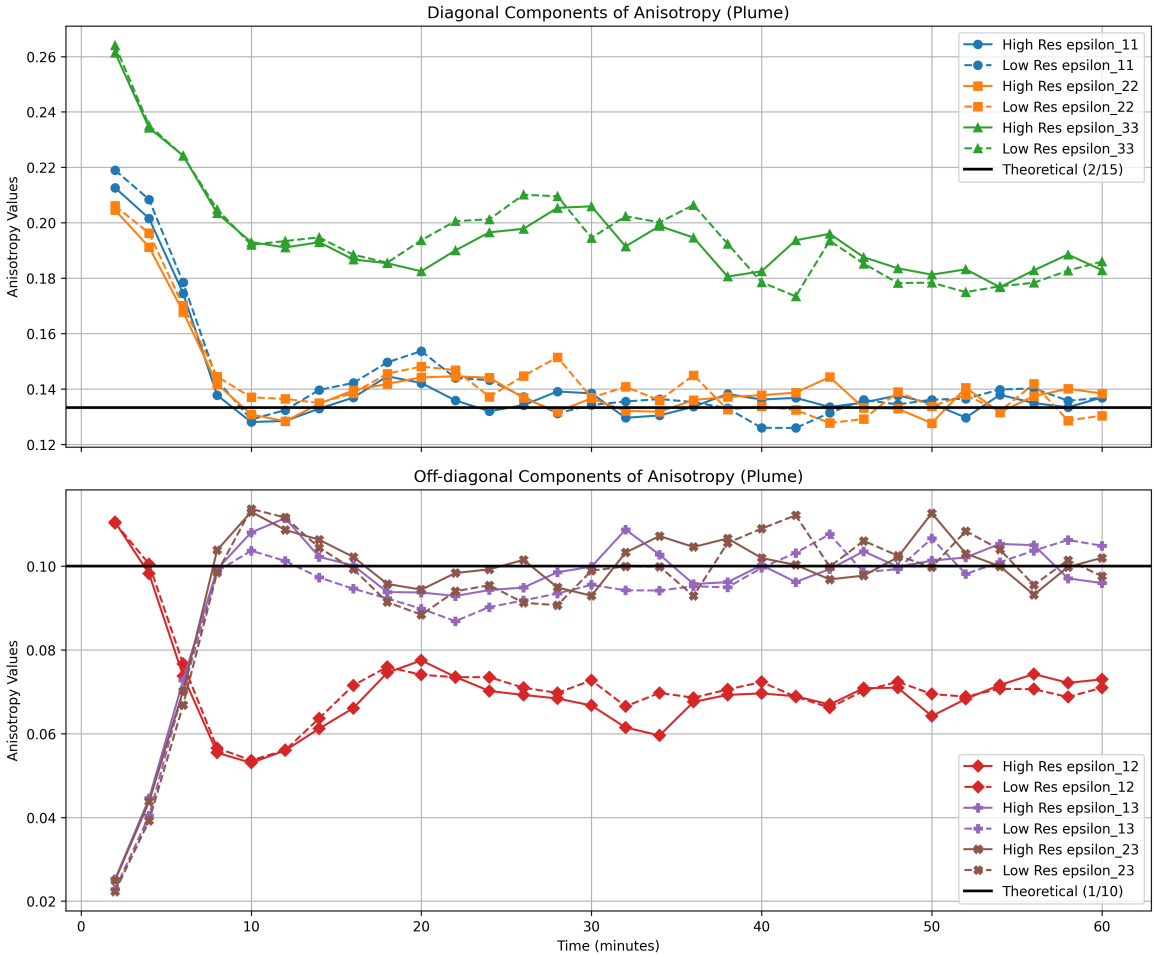


Figure 3.9: Anisotropy matrix components, ϵ_{ij}, in the plume simulation, comparing high- and low-resolution results. Top: diagonal elements with reference line at 2/15. Bottom: off-diagonal elements with reference to 1/10.

Figure 3.10 presents the evolution of the total anisotropy scalar χ_ϵ for the plume simulation, plotted in logarithmic scale. Both high and low resolution cases are shown over the full 60-minute simulation period. Initially, χ_ϵ starts at a high value for both resolutions, indicating strong anisotropy due to the absence of developed turbulence. As the simulation progresses, χ_ϵ decreases rapidly, showing the transition toward more isotropic turbulence as the plume evolves and mixes the flow. Around the 15-minute mark, both resolutions reach their lowest anisotropy levels, indicating the onset of a statistically steady turbulent state.

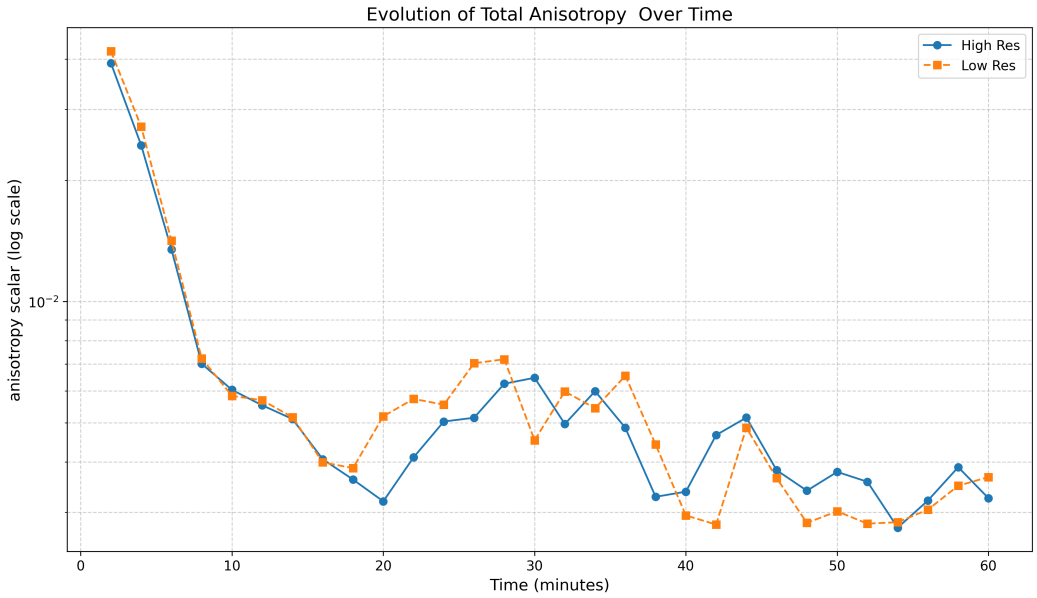


Figure 3.10: Evolution of total anisotropy χ_ϵ in log scale for high- and low-resolution plume simulations.

Beyond this point, the values fluctuate but remain in the 10^{-2} range or lower, suggesting that turbulence remains reasonably isotropic. The high-resolution case generally exhibits slightly lower χ_ϵ values throughout the latter half of the simulation, reflecting improved isotropy with higher resolution.

Figure 3.5 and Figure 3.10 compare the total anisotropy scalar χ_ϵ in the CBL and plume simulations. In both cases, anisotropy rapidly decreases at early times. However, the CBL case reaches a much lower steady value around 10^{-3}, while the plume case settles around 10^{-2}. This indicates that the CBL flow becomes more isotropic over time, especially at high resolution. In contrast, the plume retains higher levels of anisotropy throughout the simulation. These differences are because, in the plume case, there is entrainment of quiet air from outside the plume, which is an additional source of anisotropy compared to the more homogeneous CBL. Interestingly, χ_ϵ in the plume case shows much less sensitivity to grid resolution compared to the CBL case. This is likely because the plume forcing is more localized and dominant, setting a coherent structure early on that governs the turbulence evolution. Additionally, another reason for this may be that there are non-turbulent regions within the plume averaging box.

3.3 Randomly Perturbed Stratified Shear flow

The randomly perturbed simulation was designed to investigate turbulence triggered by initial perturbations in potential temperature, initialized with a perturbation. The base state is a stably stratified flow with a hyperbolic tangent initial velocity and potential temperature profile, characterized by a minimum Ri of 0.1, which ensures that shear turbulence is forming. Small-amplitude random perturbations were added throughout the domain to the potential temperature field to induce localized regions of instability. The simulation was run for 3 hours with periodic boundary conditions, which allow disturbances to freely propagate through the domain without artificial reflections.

Figures 3.11 and 3.12 show the evolution of vorticity and potential temperature for the randomly perturbed shear-driven simulation at four selected times: $t = 20$, 40, 90, and 170 minutes. These snapshots illustrate the transition from initial wave-like shear instability to fully developed turbulent mixing. At $t = 20$ minutes, the characteristic Kelvin–Helmholtz (KH) billows are clearly visible, indicating strong coherent structures in the flow. These structures are large and periodic, with strong vorticity bands centred around $z \approx 5$ km. The corresponding potential temperature contours show sharp gradients along the wave crests, clearly separating the warmer and cooler layers. By $t = 40$ min, the large billows break down into smaller-scale eddies with more irregular shapes. Vorticity becomes more scattered across the vertical extent from 4 to 7 km, and the potential temperature field shows signs of early mixing, especially at the interface around $z \approx 5$ km. This is consistent with the breakdown of coherent vorticity features, the growth of the turbulent mixing layer and KH billows, as well as the three-dimensionalization of flow. As time progresses to $t = 90$ and 170 min, the vorticity becomes more distributed and disorganized, while the temperature field reveals enhanced vertical mixing and a broader mixing layer centered around $z \approx 5$–6 km. At $t = 90$ minutes, the vorticity field appears to quiet down slightly, with less intense structures and smoother patterns. However, by $t = 170$ minutes, the vorticity increases again, indicating an increase in turbulent mixing. This pattern aligns with the broader trend of turbulence initially growing, then decaying, and re-intensifying. The potential temperature field reflects this behaviour as well: the mixing layer thickens modestly by $t = 90$ minutes but shows renewed sharp gradients and irregular structures by $t = 170$ minutes, especially between 4 and 7 km altitude. This evolution highlights the transition to turbulence driven by shear instability and the progressive homogenization of the stratified layer.

Figure 3.13 displays the time evolution of the total dissipation ε_{tot} for the high-resolution randomly perturbed shear-driven case. The values are domain-averaged over 12 km in x and 1 km in y and height. The dissipation rises sharply and reaches its peak at around

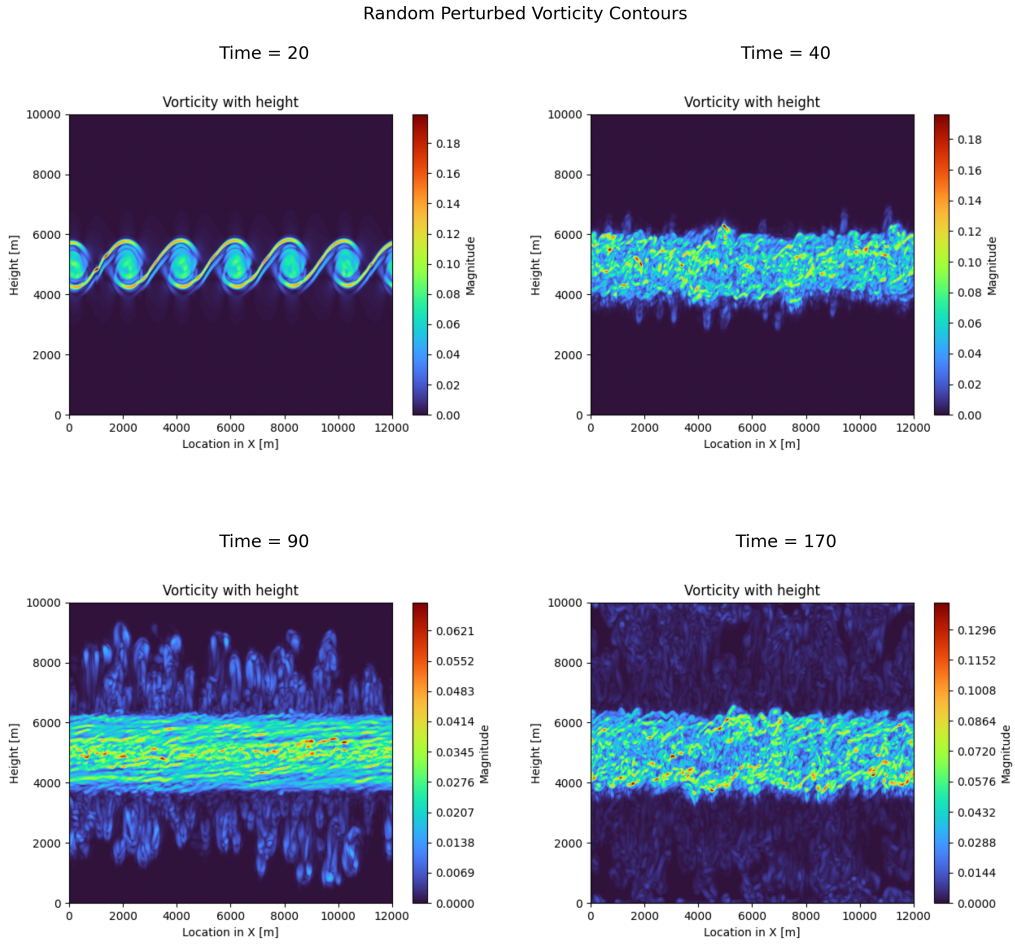


Figure 3.11: Magnitude of total vorticity contour of randomly perturbed simulation for four selected times.

27 minutes, which corresponds to the onset of strong localized turbulence triggered by the instability in the initial velocity and temperature fields. This sharp spike is followed by a rapid decay, indicating that the initial burst of turbulence transitions quickly into a more developed but weaker turbulent regime. The timing of this decay aligns with the vorticity field becoming increasingly disordered, as seen in Figures 3.11 and 3.12. After the peak, the dissipation gradually decreases and then plateaus, but a secondary rise can be observed around 150 minutes. This secondary bump might reflect a new phase of flow adjustment or the onset of additional instabilities. The overall trend suggests an initial burst of turbulence, then quiet, then a later but smaller burst of turbulence.

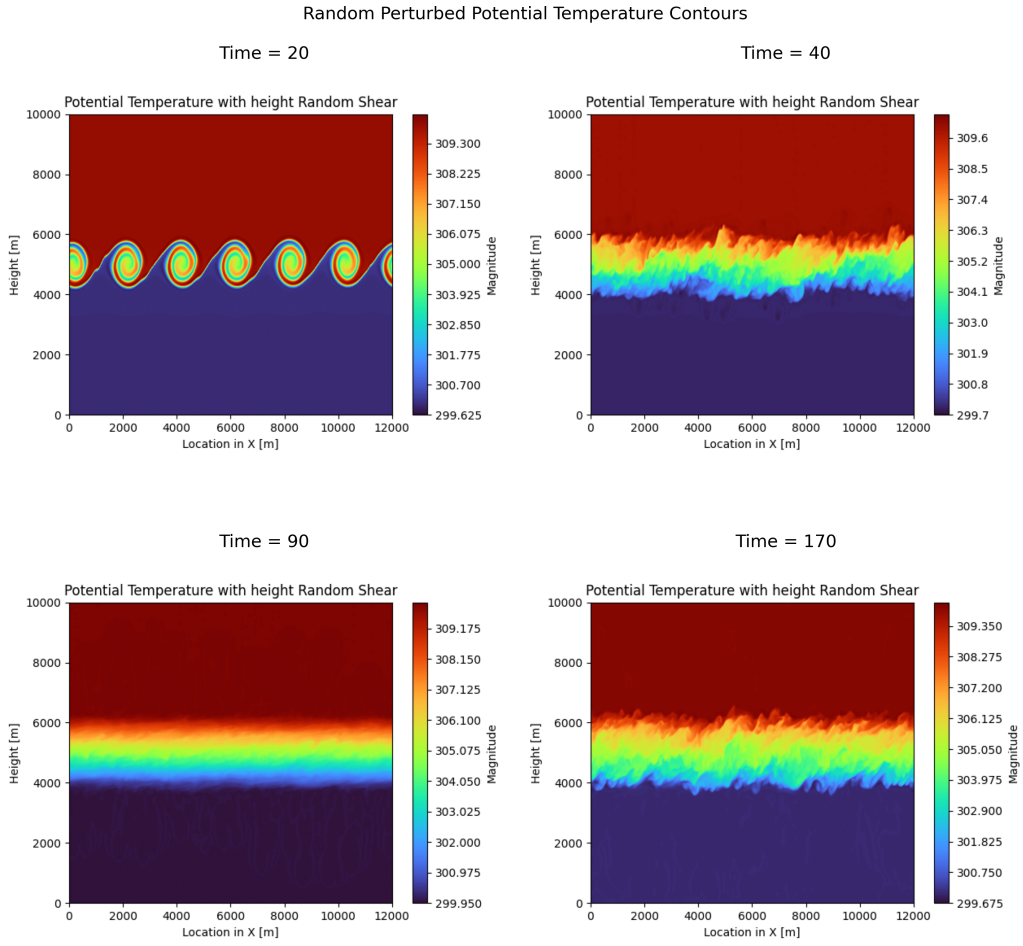


Figure 3.12: Potential Temperature contour of randomly perturbed simulation for four selected times.

For the randomly perturbed shear case, the Ozmidov scale and the shear length scale were calculated based on the initial stratification, velocity shear, and the maximum ϵ value. The Ozmidov scale is around 20 m, while the shear scale is about 100 m. This indicates that buoyancy effects act at smaller scales than shear, and both influence the structure of turbulence in this case.

Figure 3.14 shows the temporal evolution of the anisotropy matrix components for the randomly perturbed shear-driven case. The upper panel presents the diagonal components (ε_{11}, ε_{22}, ε_{33}), and the lower panel shows the off-diagonal components (ε_{12}, ε_{13}, ε_{23}), for both high-resolution and low-resolution simulations. Over time, all diagonal elements

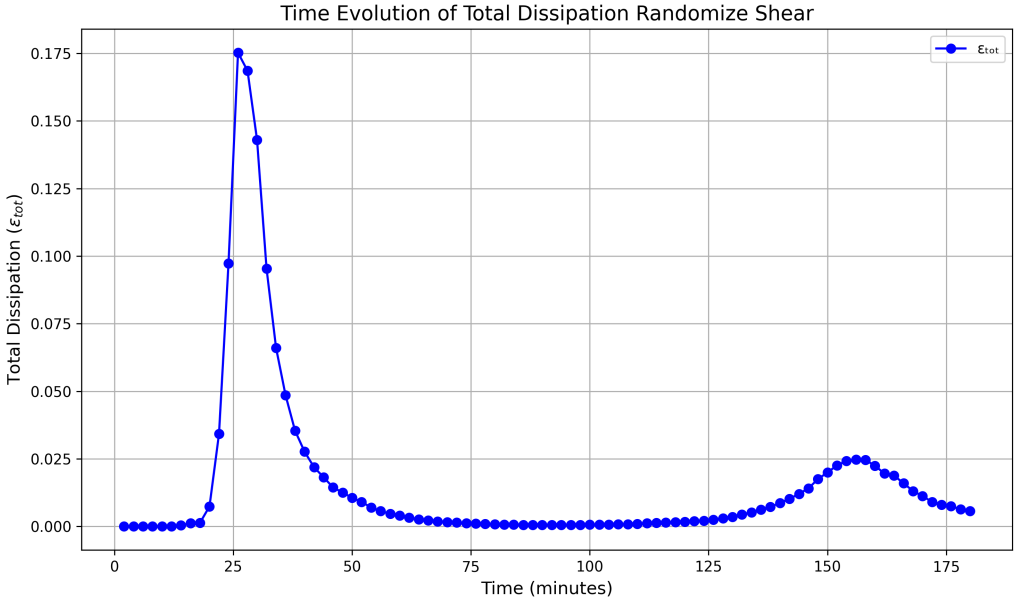


Figure 3.13: Time evolution of total dissipation rate ϵ_{tot} in the randomly perturbed simulation.

trend toward the isotropic limit, though their convergence behaviour varies. The diagonal components initially deviate significantly from the theoretical isotropic value of 2/15, showing strong anisotropy at the onset of turbulence. Between $t = 25$–50 min, ε_{22} exceeds the isotropic line while ε_{11} and ε_{33} remain below it. This suggests that vertical shear-induced motions are dominant during this period, as ε_{11} and ε_{33} can be non-zero even in a quasi-two-dimensional flow, whereas ε_{22} requires full three-dimensionalization. At later times, all components drop below the isotropic benchmark, with a secondary burst around $t = 150$ min where high-resolution ε_{22} rises above the line again. In particular, ε_{22} shows higher values than ε_{11} and ε_{33}, especially during the earlier part of the simulation. The fluctuations in ε_{22} in particular reflect persistent vertical shear effects in the mid-layer, which is consistent with the layered structure seen in temperature plots.

The off-diagonal terms ε_{13} and ε_{23} are significantly larger than the isotropic value of 1/10 during the early burst phase ($t < 25$ min), while ε_{12} remains below the benchmark. Over time, ε_{13} and ε_{23} decrease gradually but remain elevated during active mixing phases (e.g., $t = 60$–120 min). Meanwhile, ε_{12} slowly rises toward the theoretical value, indicating growing coupling in the horizontal plane. Quiet periods (e.g., $t = 30$–50 min and after $t = 130$ min) show dampened off-diagonal values across the board, consistent with reduced

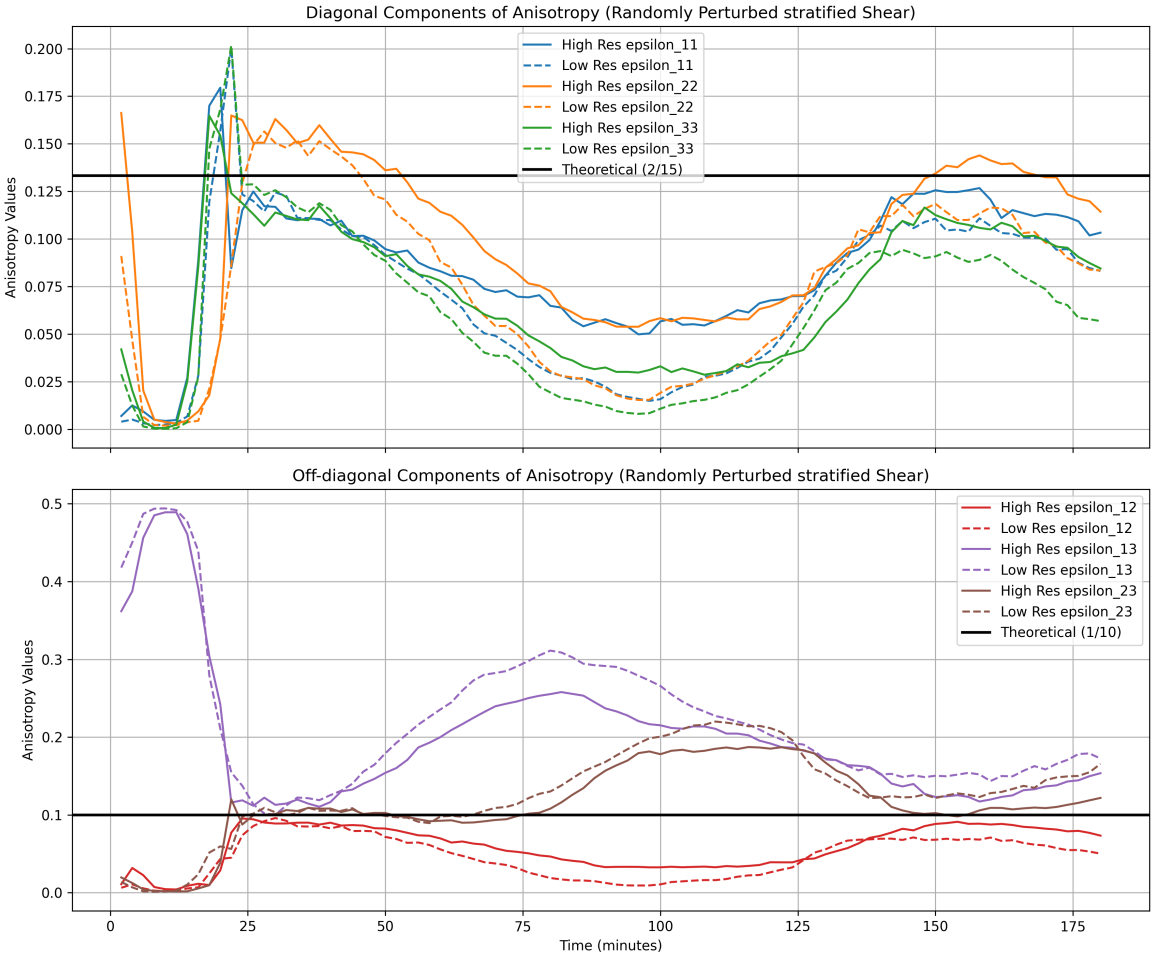


Figure 3.14: Anisotropy matrix components in the randomly perturbed simulation. Top: diagonal elements (reference line at 2/15). Bottom: off-diagonal elements (reference line at 1/10).

shear activity. These values remain elevated for a considerable duration before slowly declining toward the theoretical limit, albeit with fluctuations. This may be due to directional coupling between horizontal and vertical motions induced by stratification. Overall, the components illustrate a clear anisotropic-to-isotropic transition consistent with the decay of turbulence intensity and support the physical interpretation of localized perturbation evolving into sustained shear-driven turbulence.

Figure 3.15 presents the evolution of the total anisotropy scalar χ_ϵ over time for both

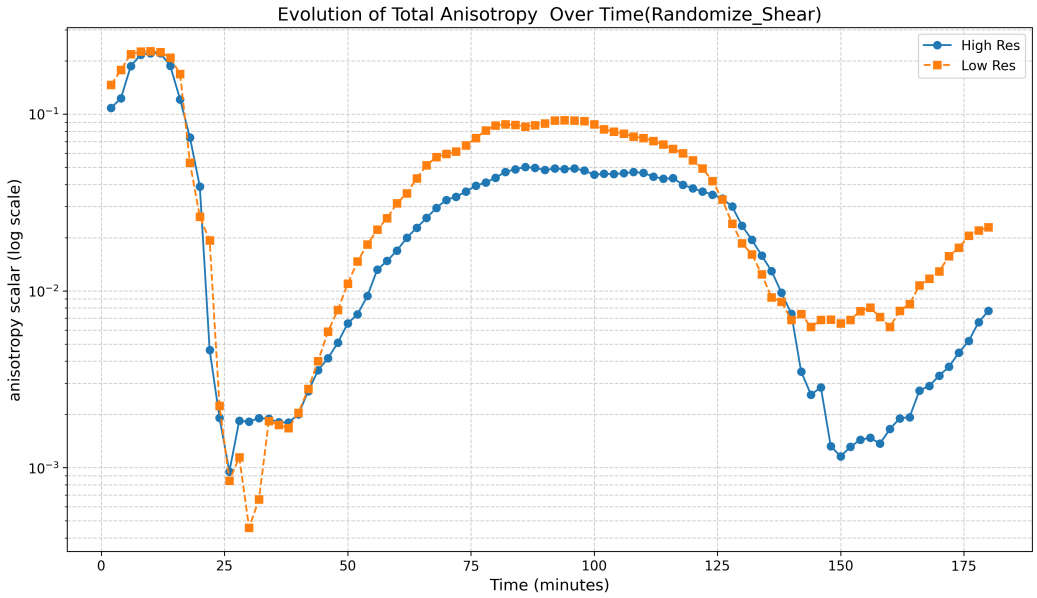


Figure 3.15: Temporal evolution of total anisotropy χ_ϵ (log scale) for high- and low-resolution randomly perturbed simulations.

high-resolution and low-resolution simulations on a logarithmic scale. At the start of the simulation, both resolutions show a steep increase in anisotropy as the initial random perturbations begin to interact with the background shear, triggering the onset of turbulence. This is followed by a rapid decay in χ_ϵ, indicating a transient phase of isotropization that matches the timing of the dissipation peak and suggests a brief isotropic phase before shear reintroduces directional effects. However, the scalar then rises again, revealing a secondary burst of anisotropy sustained by the continuous shear input that can be caused by interacting with the periodic boundary condition of the domain. Additionally, there are two periods of low χ_ϵ, corresponding to times of max ϵ, separated by a more quite period of smaller ϵ and more anisotropic dissipation.

Throughout the simulation, the high-resolution run consistently maintains lower anisotropy levels than the low-resolution counterpart, suggesting that finer spatial resolution better captures small-scale mixing and more efficiently dissipates anisotropy. The final portion of the simulation shows a slow downward trend for both cases, though low-resolution data displays greater fluctuations, potentially reflecting unresolved turbulent structures and delayed dissipation.

3.4 Locally Perturbed Stratified Shear FLow

The shear-driven simulation was designed to study turbulence generated by vertical shear in a stratified environment. The domain was initialized with a layered hyperbolic tangent potential temperature profile and a velocity profile defined by a hyperbolic tangent function, similar to the Randomly Perturbed case. This configuration creates a shear layer in the vertical direction with a minimum initial Richardson number of 0.3, which is higher than the Randomly Perturbed case to ensure localized turbulence. A thermal bubble was introduced to locally reduce the Richardson number below the critical threshold and trigger turbulence inside the bubble. The simulation was run for 1 hour using periodic boundary conditions, allowing turbulent structures to fully develop and propagate without artificial constraints at the domain boundaries.

Figures 3.16 and 3.17 show the evolution of the total vorticity and potential temperature fields for the bubble-perturbed shear flow at $t = 14$, 18, 30, and 60 minutes. These times were chosen to highlight key phases of the flow development. At $t = 14$ minutes, the vorticity field reveals a localized bubble-like region concentrated around the center of the domain, aligned horizontally near the shear interface. This localized feature is also clearly visible in the potential temperature field as a compact distortion near the same region. The strongest vorticity is tightly confined around $z \approx 5$, km and the contours show a well-defined circular structure. This matches the initial bubble injection location. By $t = 18$ minutes, the vorticity begins to spread, and small disturbances begin to stretch along the shear layer, indicating the start of shear-induced deformation and early signs of instability. The theta contours start to tilt and smear near the interface, which reflects initial vertical mixing due to bubble-shear interaction. Notably, between $t = 18$ and 30 minutes, we see a rapid transition where the initial bubble signature disappears and vorticity spreads laterally. As time progresses to $t = 30$ and 60 minutes, the vorticity becomes more dispersed across the shear zone, with no clear central bubble remaining. The perturbation has fully interacted with the background shear, producing a horizontally aligned turbulent mixing layer centered around $z \approx 5$ km. The temperature field similarly becomes more smeared out and stratified, indicating a broader mixing of the bubble with the surrounding environment. These visualizations demonstrate that the initial bubble-induced structure remains localized only up to $t \approx 14$ minutes. Afterwards, it transitions into a dispersed, shear-driven flow, losing its localized identity due to the effects of advection and turbulence. Meanwhile, the temperature field continues to show sharp gradients across the shear interface, but by $t = 60$ minutes, it becomes more layered and horizontally uniform, indicating sustained turbulent diffusion.

Figure 3.18 shows the time evolution of total dissipation ε_{tot} for the high-resolution

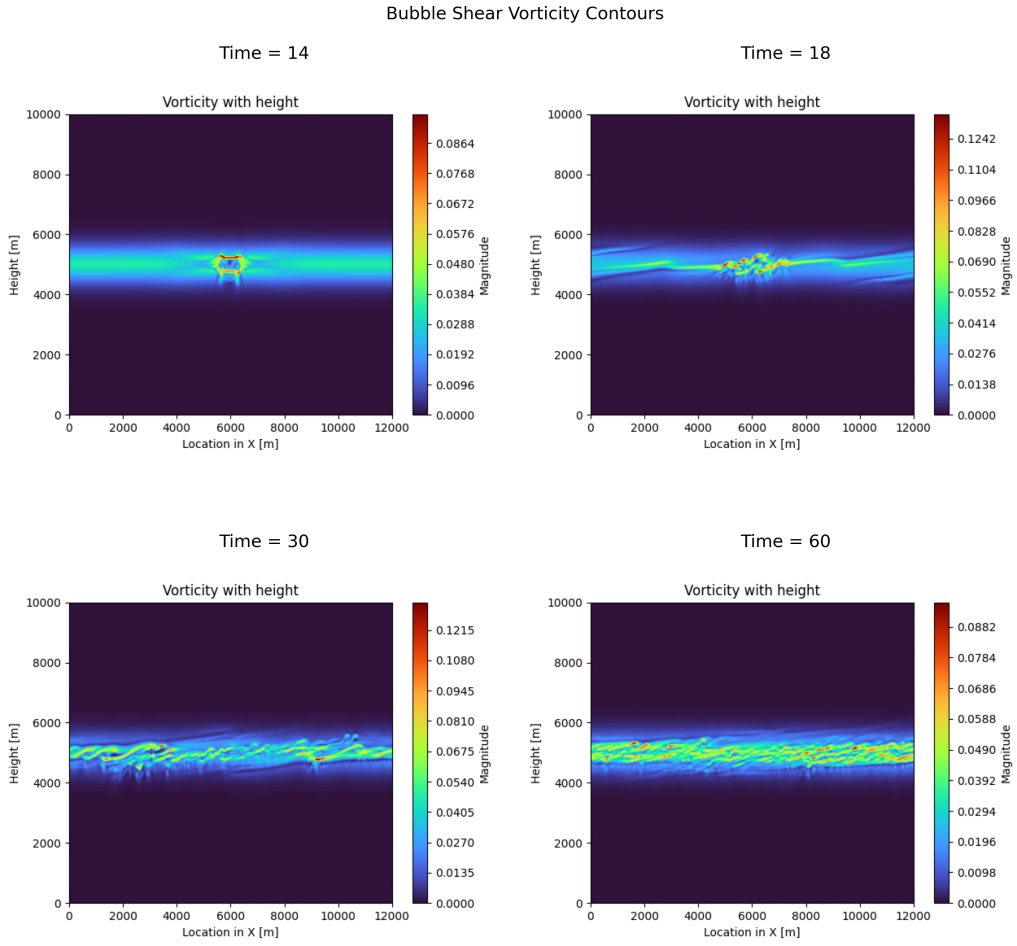


Figure 3.16: Magnitude of total vorticity contour of the shear-driven simulation for four selected times.

Localized Shear-Driven Simulation, domain-averaged over 12 km in x and 1 km in y and height. At the beginning, the dissipation remains nearly zero, indicating a calm state with minimal turbulent activity. Around $t \approx 15$ minutes, a sharp increase in ε_{tot} is observed, corresponding to the moment when the localized shear layer becomes unstable and triggers the formation of turbulent eddies. The dissipation reaches its peak near $t \approx 18$ minutes, signalling the strongest energy cascade in the flow. Following this peak, the dissipation quickly decreases as the initial burst of turbulence begins to decay. Interestingly, around $t \approx 30$ minutes, a plateau emerges, suggesting that the system reaches a quasi-stationary turbulent state with sustained low-level activity. In the later stages, the dissipation contin-

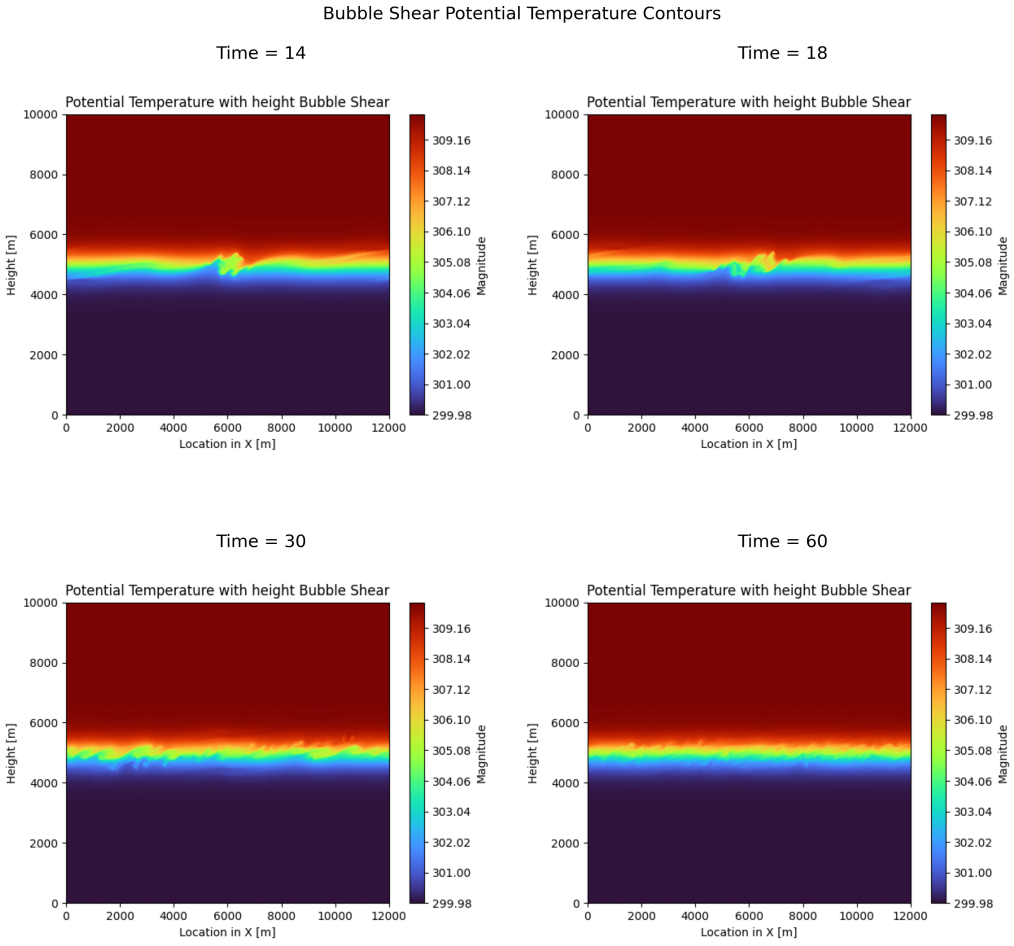


Figure 3.17: Potential temperature contour of the shear-driven simulation for four selected times.

ues a slow decline, reflecting the gradual damping of turbulence without additional forcing. Overall, the dissipation profile highlights the impulsive nature of turbulence generation due to localized shear and its subsequent decay over time.

Figure 3.19 presents the evolution of both diagonal and off-diagonal components of the anisotropy matrix for the Localized Shear-Driven Simulation. In the top panel, the diagonal components ε_{11}, ε_{22}, and ε_{33} are shown for both high- and low-resolution cases, alongside the theoretical isotropic value of $2/15$. At early times, all diagonal components are close to zero, consistent with the absence of turbulence in the initial laminar stage. As the localized shear initiates turbulence, all components rise, with ε_{22} peaking significantly above the

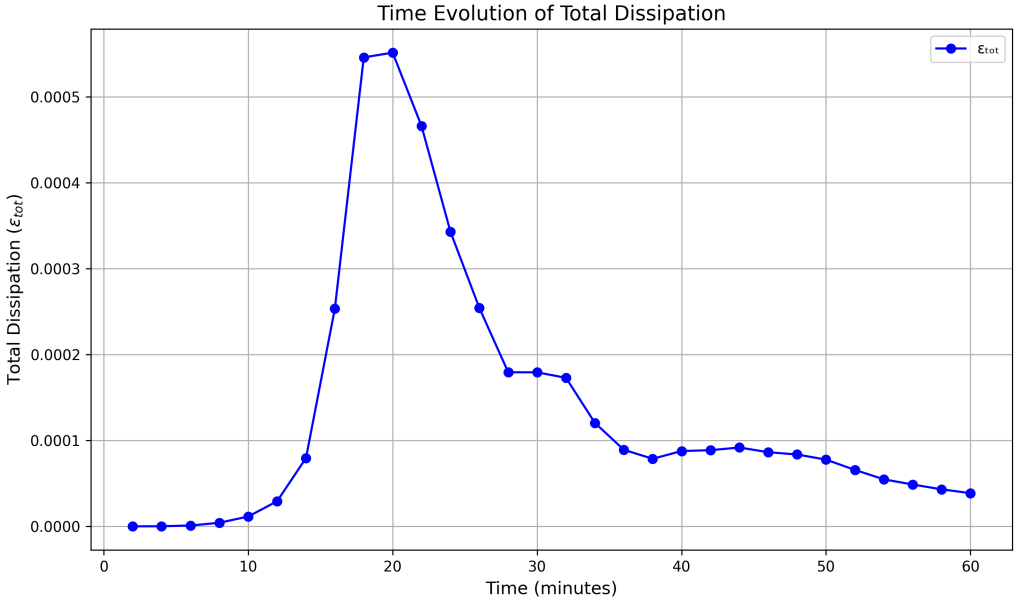


Figure 3.18: Time evolution of total dissipation rate ϵ_{tot} in the shear-driven simulation.

isotropic benchmark. In contrast, ε_{11} and ε_{33} remain well below 2/15, indicating anisotropic energy distribution that temporarily favours the span-wise direction while maintaining a mostly two-dimensional flow. After their peak, all diagonal components decrease below the isotropic value. Notably, ε_{22} stays higher than ε_{11} and ε_{33} throughout, especially in the high-resolution case, reflecting sustained spanwise anisotropy. The lower panel shows the off-diagonal components ε_{12}, ε_{13}, and ε_{23}. As expected in a shear-driven flow, ε_{13} exhibits the maximum difference from the theoretical value of 1/10 in the early and mid phases of the simulation; however, as it goes toward the maximum dissipation, it increases toward the isotropic value over time. While ε_{12} and ε_{23} remain below the isotropic line, especially in the later stages, the overall persistence of high ε_{13} values underlines the lasting imprint of the initial shear layer on the anisotropic stress distribution in the flow. The most significant deviations are seen in ε_{13}, which reaches values up to 0.45 during peak turbulence. This indicates strong streamwise–vertical coupling. After this burst, ε_{13} remains elevated compared to other components, while ε_{12} and ε_{23} exhibit relatively stable behavior with slower convergence.

Figure 3.14 and Figure 3.19 show the evolution of anisotropy matrix components for both random and bubble-perturbed shear simulations. The diagonal and off–diagonal anisotropy components evolve differently in the two shear–driven simulations. For the di-

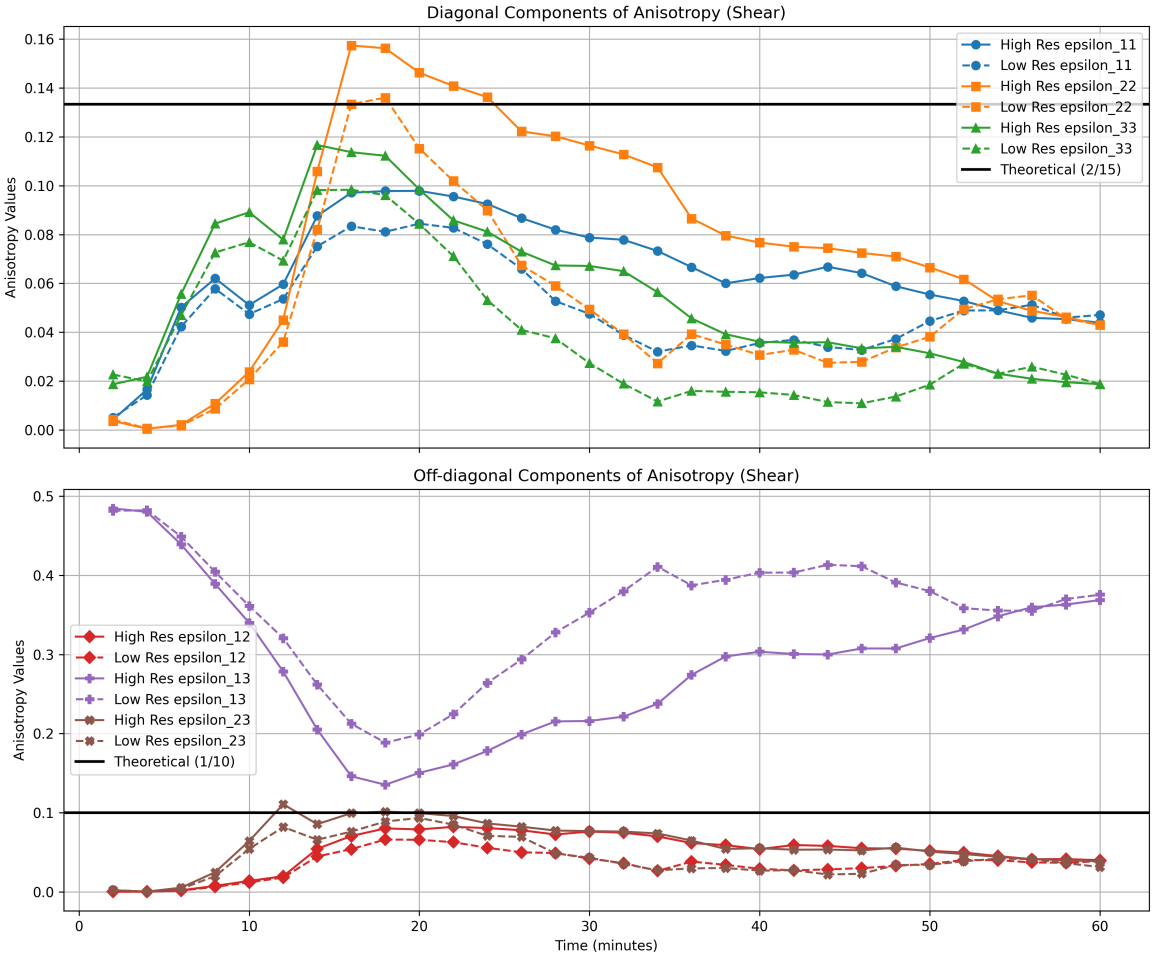


Figure 3.19: Anisotropy matrix components in the shear-driven simulation. Top: diagonal elements (reference line at 2/15). Bottom: off-diagonal elements (reference line at 1/10).

agonal terms, both ϵ_{11} and ϵ_{22} show a rapid drop near zero during the first few minutes in the randomly perturbed case, followed by a sharp rise that peaks between 20–30 minutes. After this peak, both components slowly decrease. In the bubble–perturbed case, the same components increase more gradually during the initial period, reaching their maximum values around 25–30 minutes, and then decline more smoothly. At the time of peak dissipation in the random case (around 25 minutes), ϵ_{22} exceeds the theoretical 2/15 line, while ϵ_{11} and ϵ_{33} remain well below it, highlighting strong directional energy concentration. In contrast, at the same timestamp in the bubble–perturbed case, all three diagonal components are

still rising but closer to each other, indicating a more isotropic energy distribution at this key moment.

The off–diagonal components also reveal clear differences. The ϵ_{13} component is the strongest in both test cases. At the dissipation peak of the random case, ϵ_{13} and ϵ_{23} are both significantly higher than 1/10, while ϵ_{12} stays lower. This reflects strong shear coupling in the vertical direction, while horizontal-horizontal interactions remain weaker. In contrast, during the same stage in the bubble case, ϵ_{13} and ϵ_{23} are elevated but start to flatten earlier, suggesting a more stabilized anisotropy pattern. In summary, the randomly perturbed shear simulation produces stronger and more fluctuating anisotropy across most components, especially during the early and middle stages. The bubble–perturbed shear case evolves more smoothly and reaches a more stable anisotropic state earlier. Across all components, the differences between high and low resolution are modest, but the randomly perturbed case shows somewhat greater sensitivity. Figure 3.20 shows the evolution of the

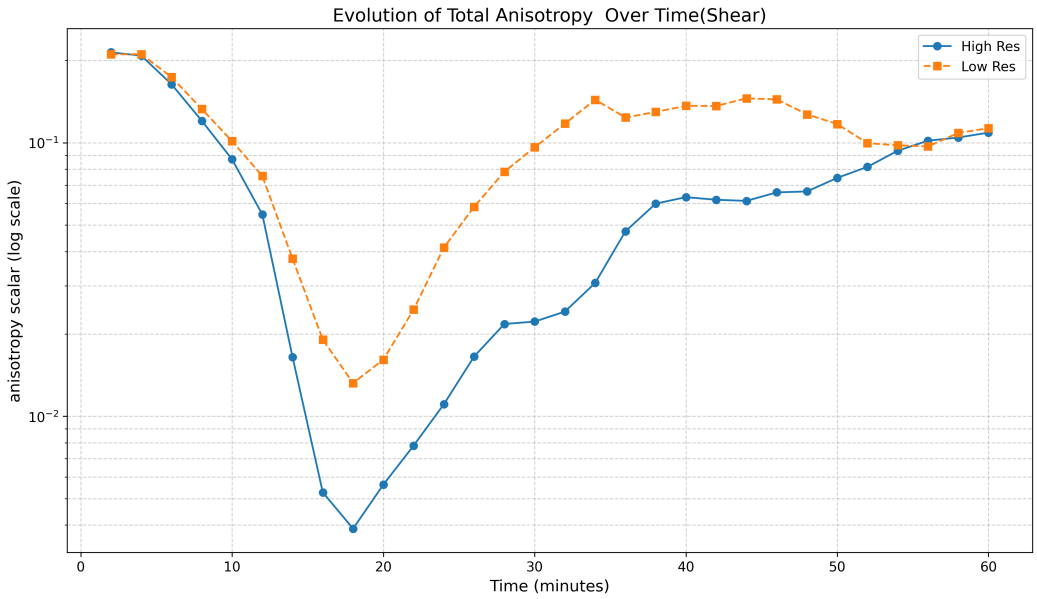


Figure 3.20: Temporal evolution of total anisotropy χ_ϵ (log scale) for high- and low-resolution shear-driven simulations.

total anisotropy scalar χ_ϵ over time for both high-resolution and low-resolution simulations under the localized shear-driven scenario. The plot is presented on a logarithmic scale to emphasize the dynamic range of anisotropy levels. Initially, both resolutions start from a relatively high anisotropy value around 0.2, which is expected due to the dominance of

laminar shear and the absence of well-developed turbulent structures. A rapid decline in χ_ϵ is observed shortly after, reaching a minimum around $t = 18$ minutes for both cases. This drop corresponds to the peak of energy dissipation, where turbulence becomes more homogeneous and the flow momentarily approaches isotropy. After this phase, χ_ϵ rises again, indicating a re-emergence of anisotropy, likely due to sustained shear production localized in certain regions. Notably, the low-resolution case maintains a consistently higher anisotropy magnitude than the high-resolution counterpart throughout the rest of the simulation. This persistent offset highlights the increased numerical dissipation and lack of small-scale resolution in the coarse grid, which limits isotropization. By the end of the simulation, both resolutions exhibit stabilized but elevated levels of anisotropy compared to their mid-simulation minima, reflecting the long-term imprint of localized shear forcing on the flow structure.

Chapter 4

Conclusion

This thesis compared how turbulence develops and behaves in four idealized simulations using the WRF model, two buoyancy-driven (CBL, Plume) and two shear-driven (Bubble-Perturbed and Random-Perturbed Shear), to investigate turbulence generation and the evolution of isotropy under different initial conditions and forcings. These cases allowed us to investigate how turbulence starts, spreads, and how isotropic it becomes over time. Across all four setups, we observed that buoyancy-driven flows (CBL and Plume) shared common features such as smoother isotropization and gradual dissipation, while shear-driven flows (Random and Bubble Shear) displayed stronger anisotropy and more intermittent turbulence bursts.

A key contribution of this work is the application of eddy viscosity-based dissipation metrics to assess isotropy, an approach modified from DNS and not previously used for eddy dissipation in LES of this type. We analyzed key metrics, including vorticity, potential temperature, total dissipation, and anisotropy components. Our comparative findings reveal distinct turbulence behaviours across cases, shaped by forcing mechanisms and resolution. Our results showed that both the forcing type and resolution level play major roles in shaping how turbulence evolves and whether it approaches isotropy. Higher spatial resolution generally improved isotropy, especially in buoyancy-driven simulations. However, in shear-driven cases, resolution alone was not always sufficient to suppress long-lived anisotropic structures.

In all cases, the total dissipation rate ε_{tot} increases rapidly during the early stages of the simulation, marking the onset of turbulence and the initial energy cascade. Although the simulations vary in duration and setup, aligning comparisons around key events, such as the first dissipation peak, helps reveal consistent patterns across forcing mechanisms.

This peak is followed by either a gradual decay or a series of fluctuations, depending on the nature of the driving mechanism. The CBL case exhibits the most prolonged growth and dissipation phase, which aligns with its continuous surface heating and gradual development of thermals, where components in the vertical direction show the most anisotropic behaviour. In contrast, the Random Perturbation and Local Bubble Perturbation simulations reach peak dissipation quickly due to the imposed velocity gradients and then exhibit a more abrupt decay or oscillatory behaviour, where horizontal components are the most anisotropic terms. The Plume case, driven by buoyancy from a localized source, demonstrates an intermediate dissipation profile, with clear evidence of transient turbulent bursts.

The total anisotropy scalar χ_ϵ consistently shows a high initial value across all simulations, reflecting the strong directional bias present in the early, structured stages of flow. Following the dissipation peak, anisotropy generally decays as turbulent mixing promotes isotropization. This decay is most pronounced in high-resolution simulations, which better capture small-scale eddies and the cascade of energy to isotropic dissipation scales. Low-resolution runs consistently retain higher anisotropy levels throughout the simulation, indicating limited mixing and persistent large-scale structures. Buoyancy-driven flows demonstrated smoother and more monotonic decay in χ_ϵ, while shear-driven flows showed greater fluctuations and slower transitions. These differences reflect the sustained directional forcing present in shear setups versus the more diffusive nature of buoyant mixing.

A component-wise analysis of the anisotropy matrix further supports these trends. Diagonal components generally approach the theoretical value of 2/15, while off-diagonal components tend toward 1/10, particularly in the buoyancy-driven CBL and Plume cases. However, in the Random Perturbation and Shear simulations, the off-diagonal components such as ϵ_{13} and ϵ_{23} remain elevated at late times, especially at low resolution. This indicates sustained anisotropy driven by shear forces. Overall, our findings reinforce that initial conditions, forcing mechanisms, and resolution shape turbulence evolution. Buoyancy-driven flows more consistently approach isotropy, while shear-driven flows exhibit longer-lasting anisotropy. High resolution improves isotropy, though its effect is more limited in strongly sheared flows.

For future work, we recommend testing alternative ways of measuring anisotropy to validate our findings. Potential methods include analyzing energy spectra to assess isotropy across different velocity scales, and applying the Lumley triangle framework to investigate large-scale Reynolds stress anisotropy, as described by Lang and Waite [2019]. It would also be useful to explore more realistic boundary conditions and environmental setups to bridge the gap between idealized and real-world applications. In particular, studying stationary

versus transient turbulent regimes may help explain the time-varying anisotropy patterns seen in idealized cases. Additionally, comparing results across different sub-grid scale closures, such as the regular versus dynamic Smagorinsky models, may help quantify how dissipation modelling influences isotropy trends. Lastly, pushing for even higher resolution simulations could help uncover finer-scale turbulence dynamics that were beyond the scope of this study.

References

Gary A. Briggs. Analytical parameterizations of diffusion: The convective boundary layer. *Journal of Applied Meteorology and Climatology*, 24(11):1167 – 1186, 1985. doi: 10.1175/1520-0450(1985)024⟨1167:APODTC⟩2.0.CO;2.

Douglas W. Carter and Filippo Coletti. Scale-to-scale anisotropy in homogeneous turbulence. *Journal of Fluid Mechanics*, 827:250–284, 2017. doi: 10.1017/jfm.2017.496.

Marcelo Chamecki and Nelson Dias. The local isotropy hypothesis and the turbulent kinetic energy dissipation rate in the atmospheric surface layer. *Quarterly Journal of the Royal Meteorological Society*, 130:2733 – 2752, 12 2006. doi: 10.1256/qj.03.155.

Subharthi Chowdhuri and Tirtha Banerjee. Quantifying small-scale anisotropy in turbulent flows. *Phys. Rev. Fluids*, 9:074604, Jul 2024. doi: 10.1103/PhysRevFluids.9.074604.

James W. Deardorff. Stratocumulus-capped mixed layers derived from a three-dimensional model. *Boundary-Layer Meteorology*, 18, 1980. doi: 10.1007/BF00119502.

Salma M. Elsherif and Ahmad F. Taha. Climate science and control engineering: Insights, parallels, and connections, 2025.

Uriel Frisch. *Turbulence: The Legacy of A. N. Kolmogorov*. Cambridge University Press, 1995.

Jochen Fröhlich, Jordan A Denev, Christof Hinterberger, and Henning Bockhorn. On the impact of tangential grid refinement on subgrid-scale modelling in large eddy simulation. In *International Conference on Numerical Methods and Applications*, pages 550–557. Springer, 2006.

Massimo Germano, Ugo Piomelli, Parviz Moin, and William H. Cabot. A dynamic subgrid-scale eddy viscosity model. *Physics of Fluids A: Fluid Dynamics*, 3(7):1760–1765, 07 1991. ISSN 0899-8213. doi: 10.1063/1.857955.

Stewart Glegg and William Devenport. Turbulent flows. In Stewart Glegg and William Devenport, editors, *Aeroacoustics of Low Mach Number Flows*, pages 185–220. Academic Press, 2017. ISBN 978-0-12-809651-2. doi: https://doi.org/10.1016/B978-0-12-809651-2.00009-6.

David A. Hebert and Stephen M. de Bruyn Kops. Relationship between vertical shear rate and kinetic energy dissipation rate in stably stratified flows. *Geophysical Research Letters*, 33(6), 2006. doi: https://doi.org/10.1029/2005GL025071.

Louis N. Howard. Note on a paper of John W. Miles. *Journal of Fluid Mechanics*, 10(4): 509–512, 1961. doi: 10.1017/S0022112061000317.

Nikolaos D. Katopodes. Turbulent flow. In Nikolaos D. Katopodes, editor, *Free-Surface Flow*, pages 566–650. Butterworth-Heinemann, 2019. ISBN 978-0-12-815489-2. doi: https://doi.org/10.1016/B978-0-12-815489-2.00008-3.

A. N. Kolmogorov. The local structure of turbulence in incompressible viscous fluid for very large Reynolds numbers. *Dokl. Akad. Nauk SSSR*, 301, 1941.

C. J. Lang and Michael L. Waite. Scale-dependent anisotropy in forced stratified turbulence. *Physical Review Fluids*, 4(4), 2019. ISSN 2469990X. doi: 10.1103/PhysRevFluids.4.044801.

Adrien Lefauve and P.F. Linden. Experimental properties of continuously forced, shear-driven, stratified turbulence. part 1. mean flows, self-organisation, turbulent fractions. *Journal of Fluid Mechanics*, 937:A34, 2022. doi: 10.1017/jfm.2021.810.

D. Lopes, H. Puga, J. Teixeira, R. Lima, J. Grilo, J. Dueñas-Pamplona, and C. Ferrera. Comparison of RANS and LES turbulent flow models in a real stenosis. *International Journal of Heat and Fluid Flow*, 107:109340, 2024. ISSN 0142-727X. doi: https://doi.org/10.1016/j.ijheatfluidflow.2024.109340.

J.B. Marston and Steven Tobias. Recent developments in theories of inhomogeneous and anisotropic turbulence. *Annual Review of Fluid Mechanics*, 55, 10 2022. doi: 10.1146/annurev-fluid-120720-031006.

Charles Meneveau and Joseph Katz. Scale-invariance and turbulence models for large-eddy simulation. *Annual Review of Fluid Mechanics*, 32(Volume 32, 2000):1–32, 2000. ISSN 1545-4479. doi: https://doi.org/10.1146/annurev.fluid.32.1.1.

John W. Miles. On the stability of heterogeneous shear flows. *Journal of Fluid Mechanics*, 10(4):496–508, 1961. doi: 10.1017/S0022112061000305.

Samuele Mosso, Karl Lapo, and Ivana Stiperski. Revealing the drivers of turbulence anisotropy over flat and complex terrain: an interpretable machine learning approach, 2025.

Balaji Muralidharan and Suresh Menon. A consistent multi-level subgrid scale closure for large eddy simulation of compressible flow using adaptive mesh refinement. *Computers Fluids*, 180:159–175, 2019. ISSN 0045-7930. doi: https://doi.org/10.1016/j.compfluid.2018.12.012.

Stephen B. Pope. *Turbulent Flows*. Cambridge University Press, 2000.

Alain Pumir, Haitao Xu, and Eric D. Siggia. Small-scale anisotropy in turbulent boundary layers. *Journal of Fluid Mechanics*, 804:5–23, 2016. doi: 10.1017/jfm.2016.529.

Elmar R. Reiter and Anne Burns. The structure of clear-air turbulence derived from "TOPCAT" aircraft measurements. *Journal of Atmospheric Sciences*, 23(2):206 – 212, 1966. doi: 10.1175/1520-0469(1966)023⟨0206:TSOCAT⟩2.0.CO;2.

Lewis F Richardson. *Weather prediction by numerical process*. Franklin Classics, 1922.

Serena Sirigu, Roberto Corona, Nicola Montaldo, John D. Albertson, and Gabriel G. Katul. Spectral distortions to momentum and scalar exchanges by non-turbulent motion and patchy landscape variability. *Agricultural and Forest Meteorology*, 371:110546, 2025. ISSN 0168-1923. doi: https://doi.org/10.1016/j.agrformet.2025.110546.

William C Skamarock, Joseph B Klemp, Jimy Dudhia, David O Gill, Zhiquan Liu, Judith Berner, Wei Wang, Joseph G Powers, Michael G Duda, Dale M Barker, and Xin-Zhong Huang. A description of the advanced research WRF model version 4. Technical Report NCAR/TN-556+STR, National Center for Atmospheric Research, 2019.

J. Smagorinsky. General circulation experiments with the primitive equations: I. The basic experiment. *Monthly Weather Review*, 91(3):99 – 164, 1963. doi: 10.1175/1520-0493(1963)091⟨0099:GCEWTP⟩2.3.CO;2.

William Smyth and Jim Moum. Length scales of turbulence in stably stratified mixing layers. *Physics of Fluids*, 12, 12 2000. doi: 10.1063/1.870385.

Ivana Stiperski and Marc Calaf. Dependence of near-surface similarity scaling on the anisotropy of atmospheric turbulence. *Quarterly Journal of the Royal Meteorological Society*, 144, 12 2017. doi: 10.1002/qj.3224.

Ivana Stiperski, Marc Calaf, and Mathias Rotach. Scaling, anisotropy and complexity in near-surface atmospheric turbulence. 09 2018. doi: 10.31223/osf.io/cj3qw.

Ivana Stiperski, Marcelo Chamecki, and Marc Calaf. Anisotropy of unstably stratified near-surface turbulence. *Boundary-Layer Meteorology*, 180(3):363–384, 2021.

Roland Stull. The atmospheric boundary layer. In John M. Wallace and Peter V. Hobbs, editors, *Atmospheric Science (Second Edition)*, pages 375–417. Academic Press, San Diego, second edition edition, 2006. ISBN 978-0-12-732951-2. doi: https://doi.org/10.1016/B978-0-12-732951-2.50014-4.

Rohit Supekar and Thomas Peacock. Interference and transmission of spatiotemporally locally forced internal waves in non-uniform stratifications. *Journal of Fluid Mechanics*, 866:350–368, 2019. doi: 10.1017/jfm.2019.106.

Bruce R. Sutherland, Ulrich Achatz, Colm-cille P. Caulfield, and Jody M. Klymak. Recent progress in modeling imbalance in the atmosphere and ocean. *Phys. Rev. Fluids*, 4: 010501, Jan 2019. doi: 10.1103/PhysRevFluids.4.010501.

Geoffrey Ingram Taylor. Statistical theory of turbulenc. *Proceedings of the Royal Society of London. Series A - Mathematical and Physical Sciences*, 151(873):421–444, 1935. doi: 10.1098/rspa.1935.0158.

Riccardo Togni, Andrea Cimarelli, and Elisabetta De Angelis. Resolved and subgrid dynamics of Rayleigh–Bénard convection. *Journal of Fluid Mechanics*, 867:906–933, 2019. doi: 10.1017/jfm.2019.119.

Guichao Wang, Fan Yang, Ke Wu, Yong-Feng Ma, Cheng Peng, Tianshu Liu, and Lian-Ping Wang. Estimation of the dissipation rate of turbulent kinetic energy: A review. *Chemical Engineering Science*, 229:116133, 01 2021. doi: 10.1016/j.ces.2020.116133.

Z. Warhaft. Passive scalars in turbulent flows. *Annual Review of Fluid Mechanics*, 32(Volume 32, 2000):203–240, 2000. ISSN 1545-4479. doi: https://doi.org/10.1146/annurev.fluid.32.1.203.

Tomoaki Watanabe and Koji Nagata. The response of small-scale shear layers to perturbations in turbulence. *Journal of Fluid Mechanics*, 963:A31, 2023. doi: 10.1017/jfm.2023.316.

Louis J Wicker and William C Skamarock. Time-splitting methods for elastic models using forward time schemes. *Monthly weather review*, 130(8):2088–2097, 2002.

John C. Wyngaard. *Turbulence in the Atmosphere*. Cambridge University Press, 2010.

Cheng-Nian Xiao and Inanc Senocak. Impact of stratification mechanisms on turbulent characteristics of stable open-channel flows. *Journal of the Atmospheric Sciences*, 79(1): 205 – 225, 2022. doi: 10.1175/JAS-D-21-0063.1.

Naoto Yokoyama and Masanori Takaoka. Energy-based analysis and anisotropic spectral distribution of internal gravity waves in strongly stratified turbulence. *Physical Review Fluids*, 4(10):104602, 2019.